

# Thiol-rich and ion-imprinted alginate hydrogel as a highly adsorptive and recyclable filtration membrane for rapid and selective Sr(II) removal

Botuo Zheng<sup>#,a</sup>, Jiajia Yin<sup>#,a</sup>, Lingdan Zhu<sup>a</sup>, Bingnan Zhou<sup>a</sup>, Hang Shen<sup>b</sup>, David Harbottle<sup>c</sup>, Timothy N. Hunter<sup>c</sup>, Yu Sheng<sup>a</sup>, Deqin Zhu<sup>a</sup>, Huagui Zhang<sup>a,d,\*</sup>

<sup>a</sup> College of Chemistry and Materials Science, Fujian Key Laboratory of Polymer Materials, Fujian Normal University, Fuzhou 350007, China

<sup>b</sup> College of Materials and Chemical Engineering, Minjiang University, Fuzhou 350108, China

<sup>c</sup> School of Chemical and Process Engineering, University of Leeds, Leeds LS2 9JT, United Kingdom

<sup>d</sup> Institute of Physical Chemistry, RWTH Aachen University, Landoltweg 2, Aachen 52056, Germany

## Abstract

Radioactive metal ion such as strontium ion,  $^{90}\text{Sr}^{2+}$ , has posed severe threats to environments and humans since the wide application of nuclear power plants around the world, while a rapid remediation of  $\text{Sr}^{2+}$  contaminated water still remains challenging. The current study developed an economical biomaterial-based hydrogel adsorbent with excellent  $\text{Sr}^{2+}$  adsorption performance achieved by ion-imprinting and abundant thiol groups, which was adaptable as an adsorptive filtration membrane for efficient and rapid purification of  $\text{Sr}^{2+}$  polluted water.

The hydrogel was synthesized via a three-step route based on sodium alginate (SA). First, SA was emulsified and converted via  $\text{Sr}^{2+}$  complexation to hydrogel (SA-Sr); secondly, a thiol-rich carboxyethyl grafted pentaerythritol tetrakis (thioglycolic acid) ester (PA) synthesized by click chemistry was used to covalently crosslink the hydrogel (SA-PA-Sr) with abundant thiol groups simultaneously introduced. Lastly, a  $\text{Sr}^{2+}$ -imprinted adsorbent (SA-PA-H) was obtained via acid elution of the SA-PA-Sr gel.

The SA-PA-H was demonstrated to exhibit a superior  $\text{Sr}^{2+}$  adsorption capacity ( $\sim 151.7$  mg/g), a rapid adsorption kinetics following pseudo-second order with a rate constant of  $0.669$  g  $\text{mg}^{-1}$   $\text{min}^{-1}$ , decent selectivity for  $\text{Sr}^{2+}$ , a value  $\sim 1.14 \times 10^3$  mL  $\text{g}^{-1}$  when adsorbing 10 ppm  $\text{Sr}^{2+}$  from

30 concentrated (100 ppm) solutions of competitive ions ( $\text{Na}^+$  or  $\text{Mg}^{2+}$ ). The good performance was  
31 maintained over a wide range of pH (4-10) and temperature (25-40 °C), and the adsorption  
32 mechanism was attributed to the prevalent  $\text{Sr}^{2+}$  bindings to thiol groups and  $\text{Sr}^{2+}$ -imprinted cavities.  
33 Moreover, high elasticity with a storage shear modulus  $\sim 10$  MPa at low strains whilst rapid and  
34 full self-recovery after being repeatedly damaged by large strains of the SA-PA-H were  
35 demonstrated by rheology. This allowed the SA-PA-H to be adapted as a membrane for vacuum  
36 filtration, giving a high removal efficiency ( $> 99.2\%$ ) of  $\text{Sr}^{2+}$  under a high liquid flux ( $\sim 40 \text{ L m}^{-2}$   
37  $\text{h}^{-1}$ ). In addition, the adsorbent can be regenerated by acid washing and after four consecutive  
38 adsorption-desorption cycles, the drop in removal efficiency was minor (53.51% to 36.88% for  
39 100 ppm  $\text{Sr}^{2+}$ ). This investigation demonstrated a novel hydrogel adsorbent advantageous in cost,  
40 performance, processability, and sustainability, being applicable for rapid and complete  
41 decontamination of nuclear wastewater via adsorptive membrane filtration.

42

43 **Keywords** Ion-imprinting; alginate; strontium; adsorption; thiol; membrane; hydrogel

44

## 45 **1 Introduction**

46  $^{90}\text{Sr}$  (Strontium ( $^{90}\text{Sr}$ )) is one of the major products of nuclear fission, possessing a long half-life  
47 (28.79 years) with high energy  $\beta$ -decay. Moreover, its cation, i.e.  $^{90}\text{Sr}^{2+}$ , is highly soluble in water.  
48 Hence, if released,  $^{90}\text{Sr}^{2+}$  poses severe threats to the environment and human bodies.[1] Due to its  
49 similar chemical properties to calcium,  $\text{Sr}^{2+}$  is prone to enrich in human bodies, especially in  
50 bones. The good affinity of  $^{90}\text{Sr}^{2+}$  to bones prevents it from being excreted by metabolism like  
51 other poisons. It was demonstrated that people suffered from obvious risks of osteosarcoma, soft  
52 tissue cancer and leukemia when exposed to radioactive  $^{90}\text{Sr}$ . [2] With the wide application of  
53 nuclear power around the world, how to treat polluted water containing radioactive ions including  
54  $^{90}\text{Sr}^{2+}$  has become an urgent problem. On the other hand, Sr and its derivatives are important metal  
55 materials and have been widely used in ceramics, coatings, electronics and pharmaceuticals.[3-7]  
56 Development of efficient approaches to separating and recovering  $\text{Sr}^{2+}$  from polluted water not  
57 only protects humans and the environment but also generates significant economic benefits.

58 Researchers have developed several methods to separate metal ions from polluted water, such

59 as chemical precipitation,[8] extraction[9], floatation[10, 11], adsorption[11-14] and ion  
60 exchange[15, 16]. The methods have different removal efficiency and application scenes  
61 according to their mechanism. Among them, adsorption is considered to be one of the best ways to  
62 recover  $\text{Sr}^{2+}$  with high efficiency and various adsorptive materials are developed for the  
63 enrichment and separation of  $\text{Sr}^{2+}$ . [17-21] For example, graphene oxide which has a large specific  
64 surface area and oxygen functional groups is a good candidate for ion adsorption materials. Abu-  
65 Nada reported graphene oxide as a  $\text{Sr}^{2+}$  adsorbent in the aqueous system, with a maximum  
66 strontium adsorption capacity of 131.4 mg/g achieved. [22] Nevertheless, the traditional adsorbents  
67 for  $\text{Sr}^{2+}$ , such as polyantimonic acid, [23] sodium titanate [24] and zeolite [25-27], and nanocarbon  
68 materials [28], etc., are often prepared in form of powder with a tiny particle size (mostly in  
69 nanoscale or submicron scale), hence may cause secondary pollution when applied in water since  
70 the separation of the adsorbents are laborious. It is also difficult for the powdery adsorbents to be  
71 shaped to fit purification devices. Even though the adsorbents can be loaded to a matrix to  
72 improve their recovery abilities from water, [29, 30] the adsorption efficiency including maximum  
73 adsorption and adsorption rate generally decreases due to the loss of active adsorption sites. The  
74 relatively high cost of the adsorbent synthesis also limits its massive application. For this reason,  
75 the development of highly efficient, environment-friendly, and economical adsorbents for  $\text{Sr}^{2+}$  has  
76 attracted growing attention in the water treatment field.

77 Organic polymers usually have good stability and are easy to be functionalized by  
78 modification of monomer or polymer products. The shape of polymer adsorbent can also be  
79 tailored by various preparation techniques. The advantages have made polymers ideal candidates  
80 for adsorbents. For instance, Huh et al. synthesized a microporous covalent triazine polymer and  
81 loaded magnetite  $\text{Fe}_3\text{O}_4$  nanoparticles on it. [31] The nanocomposite served as an efficient  
82 adsorbent for the removal of strontium ion ( $\text{Sr}^{2+}$ ) from seawater with a maximum adsorption  
83 capacity of 128 mg/g. Wang et al. prepared polyaniline-functionalized porous chitosan grafted by  
84 polyacrylamide bearing sulfonic acid group and used it as  $\text{Sr}^{2+}$  adsorbent. [32] The maximum  
85 adsorption capacity was determined to be 88.95 mg/g. However, there are at least two main  
86 drawbacks hampering the wide application of polymer adsorbents. One lies in that the introduction  
87 of functional groups into polymer adsorbent for adsorption often involves extra tedious steps

88 during the synthesis of the polymers. Another is that a majority of polymers are known to be hard  
89 to degrade due to their carbon skeleton, that is, the commonly argued issue of the non-  
90 sustainability of plastics. To overcome the problem, bio-based polymer materials such as sodium  
91 alginate (SA) have been adopted as the matrix or the core adsorptive material to prepare  
92 biodegradable ion adsorbents. SA is a bio-derived polysaccharide, possessing the advantages of  
93 abundant sources, low cost, nontoxicity, and biodegradability, etc.[33, 34] SA is an excellent  
94 adsorbent for various metal ions because of abundant carboxylic side groups.[35-39] However,  
95 there is minor ion selectivity of SA towards specific ions like  $\text{Sr}^{2+}$ , which calls for further  
96 modification of SA to meet the requirement for water treatment.

97 In recent years, ion-imprinting was raised as a prominent technique to construct ion-  
98 responsive materials with selectivity to certain ions.[40] In typical ion-imprinting, the ion was first  
99 introduced as templates to complex with ligand groups in polymers. After the formation of the ion  
100 complex, crosslinking reactions were introduced via other groups on polymers to fabricate stable  
101 networks and fix the relative position of functional groups. By removing metal ions, cavities with  
102 precise shapes, sizes, and charge distribution conformed to the ion are readily created in the  
103 network. The cavities served as identification sites for the ion and thus endowed the polymer  
104 matrix with ion selectivity, which allowed the polymer to serve as an efficient adsorbent for the  
105 specific ion<sup>[41-43]</sup>. As an example of strontium recovery, Deng et al. reported a  $\text{Sr}^{2+}$ -imprinted  
106 alginate microsphere adsorbent,[44] which can successfully separate  $\text{Sr}^{2+}$  in oilfield water from  
107 other ions with a maximum adsorption capacity of 177.37 mg/g, but its microsphere form and un-  
108 crosslinking structure still make the adsorbent difficult to be recovered and unstable to be re-used.

109 Incorporating functional group with distinct affinity to the ion into the adsorbent is another  
110 effective strategy to enhance ion selectivity. Based on hard and soft Lewis acids and bases (HSAB)  
111 theory,[45] soft Lewis bases with large radii and highly deformable electron clouds are prone to  
112 combine with soft Lewis acids with similar properties. As a third-period element, sulfur was a soft  
113 Lewis base with a large radius and a thick electron cloud. Therefore, sulfur will preferentially  
114 combine with soft  $\text{Sr}^{2+}$  instead of other hard ions in a mixture of alkali and alkaline-earth metal  
115 ions including  $\text{Na}^+$ ,  $\text{Mg}^{2+}$ ,  $\text{Ca}^{2+}$ , and  $\text{Sr}^{2+}$ . Taking advantage of the feature, metal sulfides were  
116 demonstrated to be efficient adsorbents for  $\text{Sr}^{2+}$  and other soft metal ions such as  $\text{Ba}^{2+}$ ,  $\text{Co}^{2+}$  and

117 Ni<sup>2+</sup>. [46-48] Zhang et al. synthesized Na/Zn/Sn/S (NaZTS) quaternary metal sulfide nanosheets  
118 for efficient adsorption of radioactive strontium ions. [49] NaZTS exhibited ultrafast kinetics with  
119 an equilibrium time of 5 min, a broad active pH range (a removal rate of >98.4%), and a very low  
120 Sr<sup>2+</sup> desorption (< 0.04%) when employed as Sr<sup>2+</sup> adsorbent in aqueous solution. The outstanding  
121 ability of NaZTS to capture Sr<sup>2+</sup> ions was attributed to ion exchange and strong Sr-S bonding  
122 following the HSAB theory. The introduction of sulfur functional groups such as sulfonic  
123 acids [50], sulfonates [51] and thiols [44] to the adsorbent is a promising way to prepare Sr<sup>2+</sup>-  
124 selective adsorbents. Nevertheless, the traditional sulfur-containing inorganic compounds have  
125 fixed shapes and inherent brittleness, which make them difficult to be shaped and to accommodate  
126 different purification devices.

127 In this study, both the HSAB strategy and the ion-imprinting strategy were employed to  
128 develop a SA-based hydrogel adsorbent rich in thiol groups and owning Sr<sup>2+</sup>-imprinted cavities to  
129 enhance the adsorption performance and selectivity. The Sr<sup>2+</sup>-imprinted cavities were introduced  
130 by first using Sr<sup>2+</sup> to complex the carboxyl groups of SA chains, whereby SA chains were  
131 networked and thus a SA hydrogel (SA-Sr) was produced, and then ion-imprinted cavities can be  
132 obtained if the Sr<sup>2+</sup> were eliminated. However, the elimination of the Sr<sup>2+</sup> crosslinks would  
133 completely destroy the hydrogel structure. To avoid this, as well as to introduce abundant thiol  
134 groups, a thiol-functionalized tetra-arm carboxylic crosslinker PA was synthesized and used to  
135 covalently crosslink the SA-Sr hydrogel through *in situ* esterification, before the Sr<sup>2+</sup> being  
136 removed by acid elution to obtain a robust Sr<sup>2+</sup>-imprinted hydrogel (SA-PA-H). The fabrication  
137 and structure characterization of the SA-PA-H hydrogel was fully validated via a series of  
138 techniques, and its adsorption performance of Sr<sup>2+</sup> was evaluated in terms of isothermal adsorption,  
139 effect of competitive ions, time, pH and temperature, etc. Moreover, the robustness of the SA-PA-  
140 H hydrogel was assessed by rheology, and its application as adsorptive membranes for device  
141 filtration, together with its regeneration potentials were also assessed.

142

## 143 **2 Experimental**

### 144 2.1 Chemicals

145 Pentaerythritol tetrakis(mercapto acetate) (90%, PET4A), strontium chloride hexahydrate

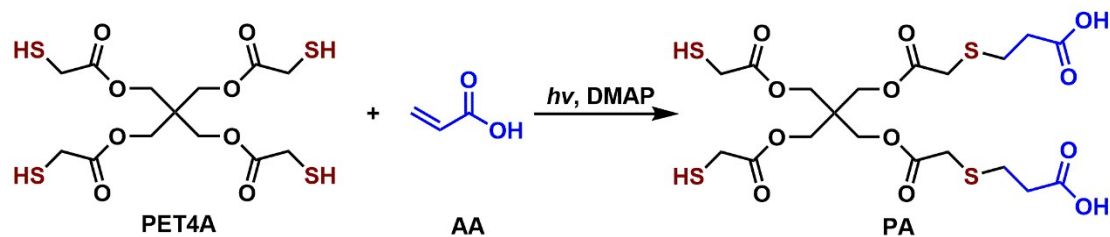
146 (99.5%,  $\text{SrCl}_2 \cdot 6\text{H}_2\text{O}$ ), dioctyl sodium sulfosuccinate sodium (96%, AOT), benzoin dimethyl ether  
147 (99%, DMPA) and sodium alginate (90%, SA) were purchased from Macklin. Acrylic acid (AA,  $\geq$   
148 99%), concentrated hydrochloric acid (36.0-38.0%), sulfuric acid (95.0-98.0%) and  
149 dichloromethane were purchased from Sinopharm Chemical Reagent Co Ltd. All the reagents  
150 were used as received.

151

## 152 2.2 Synthesis

### 153 2.2.1 Synthesis of thiol group-functionalized carboxylic modifier PA

154 PET4A (6.0076 g, 13.89 mmol), and acrylic acid (2.25 g, 31.2 mmol) were dissolved in 40  
155 mL dichloromethane followed by an addition of DMPA (0.3965 g, 1.547 mmol) as the  
156 photoinitiator. The solution contained in a round flask equipped with a water condenser was stirred  
157 and exposed to continuous UV light (250-420 nm) for 2 h. The reaction (Scheme 1) generated a  
158 mixture of PET4As functionalized with 1, 2, 3, or 4 carboxylic groups. The product was named PA  
159 and used in the following steps without further refinement.



161 Scheme 1. Synthesis of PA from photo-initiated click reaction between PET4A and acrylic acid. A  
162 typical product with two thiol groups participating in the reaction is illustrated.

163

### 164 2.2.2 Preparation of $\text{Sr}^{2+}$ complexed sodium alginate (SA-Sr) hydrogel

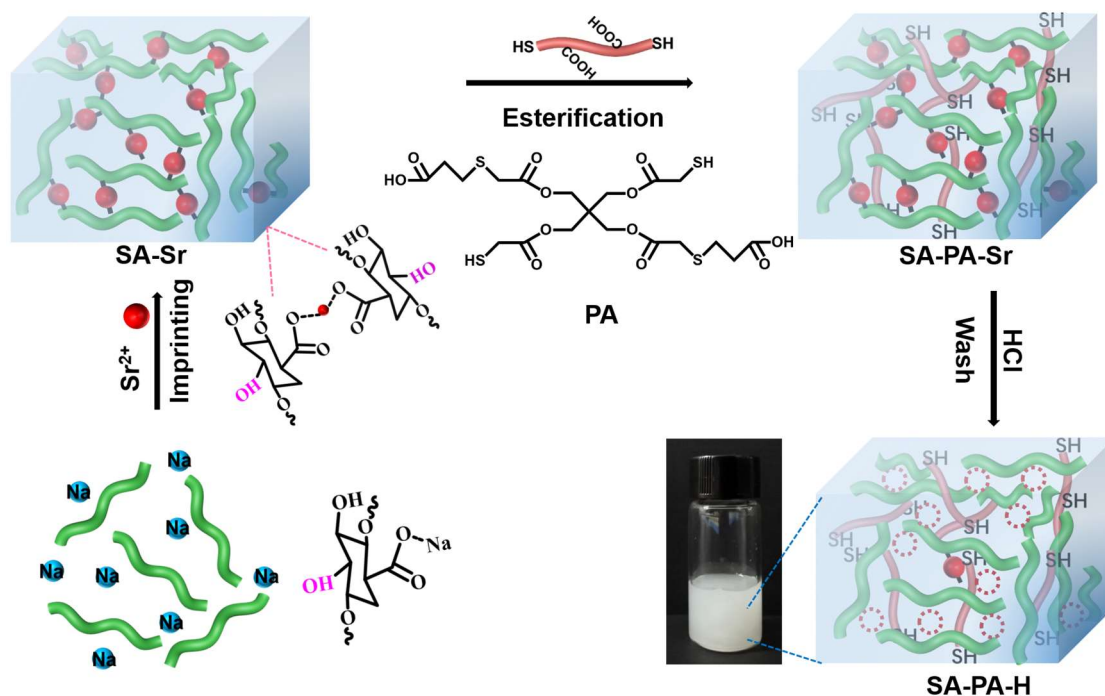
165 SA (1 g) was dissolved in 100 mL ultrapure water under stirring for 3 h to prepare a  
166 homogenous and viscous SA solution in a flask for further use. AOT surfactant (1.25 g) was  
167 dissolved in 50 mL dichloromethane followed by the addition of 25 mL of the as-prepared SA  
168 aqueous solution (1 wt%). The mixture was ultrasonicated using a Sonic Dismembrator (BILON-  
169 650Y) to prepare a W/O emulsion. Under stirring, 25 mL  $\text{Sr}^{2+}$  (0.5 wt% in water) was added  
170 dropwise and solid hydrogels precipitated from the emulsion. The mixture was stirred for 24 h to  
171 ensure full chelation between SA and  $\text{Sr}^{2+}$ , which generated an SA-Sr hydrogel. Then the emulsion

172 was centrifuged at 1000 rpm for 10 min to collect the hydrogel from the liquid and washed with  
 173 ultrapure water repeatedly to remove excess  $\text{Sr}^{2+}$ .

174

### 175 2.2.3 Fabrication of PA crosslinked and $\text{Sr}^{2+}$ -imprinted composite hydrogel (SA-PA-H)

176 About 10.0 g of the as-prepared swollen SA-Sr hydrogel (solid content 0.25 g) was re-  
 177 dispersed in 20 mL ultrapure water followed by the addition of 20 mL dichloromethane solution of  
 178 4.0 g PA. 1.6 mL  $\text{H}_2\text{SO}_4$  (0.5 wt%) was added dropwise to catalyze the esterification between the  
 179 hydroxyl groups in SA and the carboxyl groups in PA (Figure 1). After stirring for 24 h, the  
 180 chemically crosslinked hydrogel, named SA-PA-Sr, was fabricated and washed with ultrapure  
 181 water three times and separated by centrifugation at 1000 rpm for 10 min. Thereafter, the  $\text{Sr}^{2+}$   
 182 previously chelated in the hydrogel was removed by dispersing SA-PA-Sr hydrogel in 50 mL  
 183 hydrochloric acid (0.5 mol/L). The dispersion was stirred for 24 h and then washed with ultrapure  
 184 water 3 times. The composite hydrogel product named SA-PA-H was obtained with a yield of  
 185 0.197 g (solid content) and 37.2%, assuming that two monosaccharide units chelating with one  
 186  $\text{Sr}^{2+}$  was crosslinked by one PA molecules and  $\text{Sr}^{2+}$  was completely removed by acid wash. The  
 187 obtained SA-PA-H hydrogels were stored in swollen state in deionized water before use. The  
 188 synthesis procedure is illustrated in Figure 1.



189



190 Figure 1. Synthesis route of ion-imprinted thiol-functionalized SA-PA-H composite adsorbent  
191 from SA matrix, PA crosslinker and Sr. The synthesis includes three steps: (1) The chelation  
192 between  $\text{Sr}^{2+}$  and carboxylate groups in SA to prepare SA-Sr hydrogels. (2) Acid-catalyzed  
193 esterification between hydroxyl groups in SA-Sr and carboxylic groups in PA to generate thiol-  
194 functionalized cross-linked hydrogels SA-PA-Sr. (3) Preparation of ion-imprinted SA-PA-H  
195 adsorbents by washing the SA-PA-Sr hydrogels with hydrochloride acid solutions to remove  
196 chelated  $\text{Sr}^{2+}$ . The inset image displays the appearance of SA-PA-H hydrogel suspended in pure  
197 water.

198

### 199 2.3 Materials characterization

200 2.3.1 Nuclear Magnetic Resonance (NMR). NMR spectra were acquired on a Bruker AV 400M  
201 spectrometer.  $\text{CDCl}_3$  was used as the solvent with tetramethylsilane as the internal reference.

202 2.3.2 Fourier Transform Infrared (FT-IR). The infrared absorption spectra of samples were  
203 collected on a Nicolet IS50 Fourier transform infrared spectrometer (Thermo Scientific). KBr  
204 tablet methods were applied to samples. Every sample was scanned 32 times with a resolution of 4  
205  $\text{cm}^{-1}$  in the range of 400  $\text{cm}^{-1}$  to 4000  $\text{cm}^{-1}$  and the average infrared signal was adopted.

206 2.3.3 X-ray Photoelectron Spectroscopy (XPS). The sample chemical bonds were analyzed using  
207 an ESCANLAB Xi<sup>+</sup> XPS system with a monochromatic Al  $K\alpha$  X-ray source. An electron/ion gun  
208 was used to compensate for charge build-up on the sample during measurement. The XPS peaks  
209 were fitted using the CasaXPS software, and the binding energy was corrected with a reference to  
210 C 1s at 284.5 eV.

211 2.3.4 Field emission scanning electron microscopy (FE-SEM) and energy dispersive X-ray  
212 spectroscopy (EDX) mapping. The morphologies of the SA-Sr, SA-PA-Sr, and SA-PA-H samples  
213 were observed with a Hitachi Regulus 8100 cold FE-SEM coupling with EDX. The samples were  
214 sprayed with gold before the observation. The accelerating voltage was 5.0 kV and the current was  
215 10  $\mu\text{A}$ . The Octane Elect Plus X-ray spectrometer (EMAX, USA) in conjunction with SEM was  
216 used to analyze EDX elements mapping of the samples with a current of 10  $\mu\text{A}$  and an  
217 accelerating voltage of 10.0 kV.

218 2.3.5 Inductively Coupled Plasma-Optical Emission Spectroscopy (ICP-OES). The concentration  
219 of  $\text{Sr}^{2+}$  was measured by ICP-OES (Singapore, PerkinElmer) at 407.771 nm as a specific emission



220 wavelength of Sr<sup>2+</sup>. Solution samples subjected to the test were the initial Sr<sup>2+</sup> solution and  
221 supernatants collected after adsorption experiments. The concentration of Sr<sup>2+</sup> was diluted to 0-1  
222 ppm and the solution was filtered with a 0.45 µm filter before the test. The quantification was  
223 done by converting the intensities of the samples according to the standard curve established.

224

## 225 2.4 Sr<sup>2+</sup> Adsorption

### 226 2.4.1 Batch adsorption

227 All experiments were conducted using polypropylene vials to avoid Si contamination from  
228 the glassware and any potential Sr<sup>2+</sup> adsorption onto the glassware, as previously reported.<sup>10</sup> The  
229 total volume of liquid used for the adsorption was 5 mL and the solid content of hydrogel  
230 adsorbents in liquid was fixed at 1 g/L throughout all the tests. SrCl<sub>2</sub> (<sup>87</sup>Sr) was dissolved in  
231 deionized water to simulate radioactive wastewater polluted by <sup>90</sup>Sr<sup>2+</sup>. Solutions with Sr<sup>2+</sup>  
232 concentrations varying from 10 ppm to 500 ppm were prepared by diluting a 1000 ppm Sr<sup>2+</sup> stock  
233 solution. In polypropylene centrifuge tubes, suspension of hydrogel adsorbents in Sr<sup>2+</sup> solution  
234 was thoroughly mixed using an orbital shaker at 200 rpm for 24 h to promote the diffusion of Sr<sup>2+</sup>  
235 into the hydrogel. Then sample tubes were centrifuged at 11,000 rpm for 15 min, and the  
236 supernatant was decanted and passed through a 0.45 µm syringe filter. The concentration of Sr<sup>2+</sup> in  
237 the supernatant and the initial solution was determined by ICP-OES. The concentration was  
238 calibrated using SrCl<sub>2</sub> solutions of known concentrations (0, 0.1, 0.3, 0.5, 0.8 and 1 ppm) with a  
239 correlation coefficient larger than 0.999 (Figure S1).

240 The amount of Sr<sup>2+</sup> adsorbed by the solids,  $q$  (mg/g), was determined using the following  
241 equation:

$$242 \quad q = \frac{(C_o - C_e)V}{m} \quad (1)$$

243 where  $C_o$  and  $C_e$  are the initial and equilibrium Sr<sup>2+</sup> concentrations, respectively;  $V$  (L) is the  
244 volume of the suspension, and  $m$  (g) is the amount of the adsorbent (mass of solid fraction of the  
245 hydrogel).

246 Adsorption kinetics was measured at room temperature using a fixed initial Sr<sup>2+</sup> concentration  
247 ( $C_o = 100$  ppm) with a solid-to-liquid ratio of 1 g/L under neutral conditions. The concentration of  
248 Sr<sup>2+</sup> in the solution was measured at adsorption time varying from 10 min to 24 h. For

249 investigation of pH dependence, hydrogel adsorbents were tested across a pH range of 2 to 12 with  
250  $C_o = 100$  ppm. The pH was adjusted by 1.0 M HCl or 1.0 M NaOH. All other experimental  
251 parameters followed the same procedure described above.

252 The selectivity of  $Sr^{2+}$  in the presence of competitive ions was investigated by suspending 1  
253 g/L hydrogel adsorbents in solutions containing  $Sr^{2+}$  (10 ppm) with varying  $Na^+$  concentrations  
254 (100, 200, 400 and 800 ppm). After the samples were shaken for 24 h, the supernatant was  
255 separated and its  $Sr^{2+}$  concentration was determined by ICP-OES.

256

#### 257 2.4.2 Desorption of $Sr^{2+}$ and reuse of hydrogel

258 The regeneration of SA-PA-H hydrogel was investigated. For this, the hydrogel adsorbents  
259 were first subjected to  $Sr^{2+}$  adsorption experiment in  $Sr^{2+}$  solution (100 ppm) with a solid content  
260 of 1 g/L, orbital shaking at 200 rpm for 12 h to reach saturated adsorption. Then the saturated  
261 adsorbents were fully washed with ultrapure water and submerged in 100 mL hydrochloric acid  
262 (0.5 mol/L) with a solid-to-liquid ratio of 4 g/L for 6 h under stirring to remove the adsorbed  $Sr^{2+}$ .  
263 After washing and centrifuging, the regenerated hydrogel adsorbent was collected and added to a  
264  $Sr^{2+}$  solution (100 ppm) again to repeat the adsorption experiment under identical conditions (i.e.  
265 solid content 1g/L, orbital shaking at 200 rpm for 12 h). After the sorption experiments and  
266 centrifugation, the concentration of  $Sr^{2+}$  in the filtered supernatant was measured by ICP-OES to  
267 determine the adsorption capability of the regenerated adsorbent. The same procedure was  
268 repeated four times to investigate the stability and reusability of the regenerated SA-PA-H  
269 hydrogel as an adsorbent.

270

#### 271 2.4.3 Filtration test

272 Filtration membranes composed of SA-PA-H hydrogel were prepared by depositing the  
273 hydrogel at varying amounts (0.02-0.1 g) on a Nylon 6 filtration membrane with a pore size of 0.2  
274  $\mu m$  held by the sand core in a funnel with an inner diameter of 30 mm. Then the tunnel holding the  
275 SA-PA-H membrane was attached to a suction filter bottle connected to a vacuum pump. Then 100  
276 mL  $Sr^{2+}$  (0.78 ppm) solution was added to the tunnel and the pump was turned on to make a  
277 vacuum. By adjusting the pressure in the suction bottle, the  $Sr^{2+}$  solution was filtrated through the

278 membrane driven by a pressure difference across the membrane. After the filtration was completed,  
279 the filtration time was recorded to calculate the flux. The effluents were taken from the suction  
280 bottle and  $\text{Sr}^{2+}$  concentrations were determined by ICP-OES.

281

## 282 2.5 Rheology test

283 Rheological properties of the fabricated hydrogel were measured by an HR-20 stress-  
284 controlled rheometer (TA measurement, USA) with a disposable 25 mm diameter parallel plate.  
285 The geometry gap was set to 1220  $\mu\text{m}$ . A strain sweep test was first carried out at an oscillation  
286 frequency ( $\omega$ ) of 1 rad/s, and then frequency sweep tests were performed within a linear  
287 viscoelastic regime with a strain amplitude ( $\gamma$ ) of 0.5%. To investigate the relaxation/recovery  
288 behavior of the hydrogel in response to an applied shear strain, the hydrogel was subjected to an  
289 oscillation shear with following strain amplitudes and durations (in parentheses) executed in  
290 sequence: 0.1% (300 s), 1000% (300 s), 0.1% (600 s), 1000% (300 s), 0.1% (600 s), 1000% (300  
291 s), 0.1% (1200 s). The temperature was maintained at 25 °C throughout all the measurements.

292

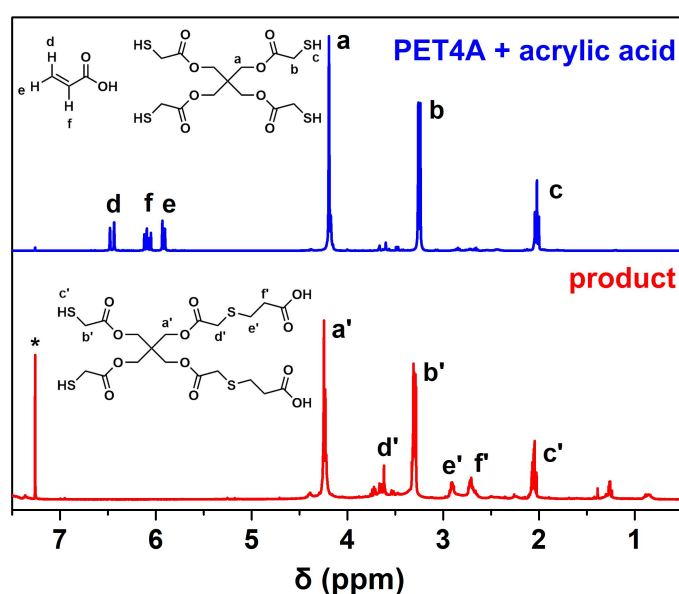
## 293 **3 Result and Discussion**

### 294 3.1 Synthesis and characterization of thiol-functionalized $\text{Sr}^{2+}$ imprinted SA hydrogels

#### 295 3.1.1 Synthesis of thiol group-functionalized crosslinker PA

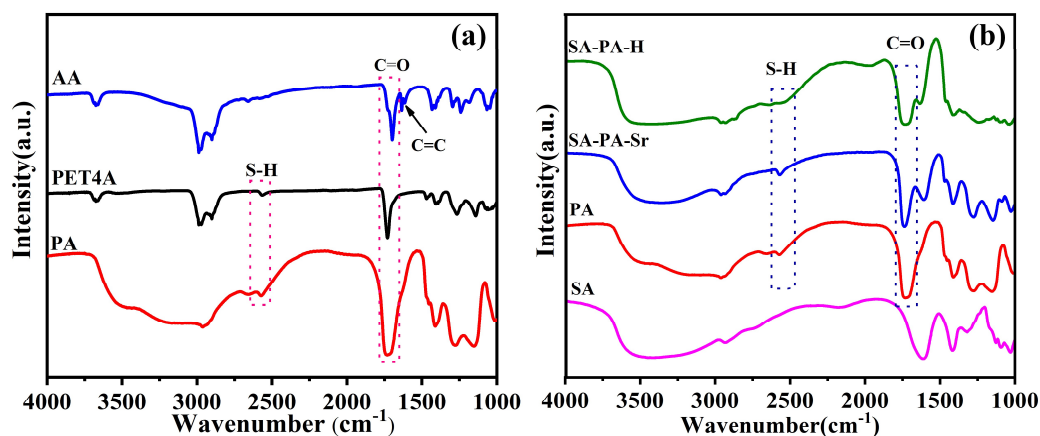
296 To develop an efficient adsorbent for  $\text{Sr}^{2+}$  removal with a high sorption capacity and  
297 selectivity, strategies of  $\text{Sr}^{2+}$  imprinting and introduction of as many thiol groups as possible to the  
298 adsorbent were considered in the present study based on sodium alginate (SA) hydrogel. To  
299 introduce thiol groups into a SA hydrogel, PET4A owing 4 thiol groups in one molecule was  
300 adopted as a crosslinker of SA via modification with acrylic acid (AA) to gain carboxylic groups  
301 for esterification with SA (Scheme 1). The modification was realized by a one-step thiol-ene click  
302 reaction between thiol groups of PET4A and about 2.2 equivalents of AA, with the product named  
303 PA (Scheme 1).  $^1\text{H}$  NMR spectra of the products and the substrate mixtures dissolved in  $\text{CDCl}_3$   
304 were compared in Figure 2. In the spectrum of substrates, signals with chemical shifts at 5.95-6.65  
305 ppm were ascribed to alkenyl protons of acrylic acids ( $\text{H}^d$ ,  $\text{H}^f$  and  $\text{H}^e$ ), which disappeared in the  
306 spectrum of PA products indicating a full conversion of acrylic acid. In the spectrum of PA product,

307 peaks ascribed to methylene protons ( $H^e$  and  $H^f$ ) near thioester and carboxylic groups at 2.71  
308 ppm and 2.93 ppm respectively are observed. At the same time, the peak at 2.06 ppm ascribed to  
309 thiol groups remained but slightly weakened after the reaction. Using the integral of  $H^a$  ( $H^{a'}$ ) as an  
310 internal standard, the conversion of the thiol group in PET4A was determined to be 34%. The  
311 results showed that an average of 1.8 thiol groups remained in every modifier/crosslinker PA  
312 molecule in the mixture product. The  $^1H$  NMR demonstrated the successful synthesis of thiol- and  
313 carboxylic-functionalized PA, being an ideal crosslinker of SA hydrogel whilst introducing a large  
314 amount of thiol groups to improve the  $Sr^{2+}$  sorption capacity of the hydrogel.



315  
316 Figure 2.  $^1H$  NMR spectra of PET4A mixed with 2.2 equiv. acrylic acid (up) and product PA  
317 dissolved in  $CDCl_3$  (bottom, \*:  $CH_3Cl$ ).

318  
319 The FTIR spectrum of PA was compared with the spectra of PET4A and acrylic acid as  
320 shown in Figure 3a. In contrast to the evident peak around  $1650\text{ cm}^{-1}$  in the AA spectrum, the  
321 characteristic adsorption of  $C=C$  disappeared in the IR spectrum of PA, which further validated the  
322 full conversion of acrylic acid. The dispersive adsorption band ascribed to O-H vibration around  
323  $3200\text{ cm}^{-1}$  increased due to the prevalent carboxylic group and adsorbed moisture in PA. The  
324 adsorption signal at  $2574\text{ cm}^{-1}$  revealed the presence of the thiol group which was also observed in  
325 the spectrum of PET4A. The FTIR spectra confirmed the synthesis of PA containing essential thiol  
326 groups to provide potential adsorption sites for  $Sr^{2+}$  when used to fabricate SA hydrogel adsorbent.



327

328 Figure 3. (a) FTIR spectra of AA, PET4A and PA. The characteristic S-H, C=O and C=C vibration  
329 adsorption peaks are highlighted by the boxes and an arrow. (b) FTIR spectra of SA, PA, SA-PA-  
330 Sr and SA-PA-H. The characteristic S-H and C=O vibration adsorption peaks are highlighted by  
331 the boxes.

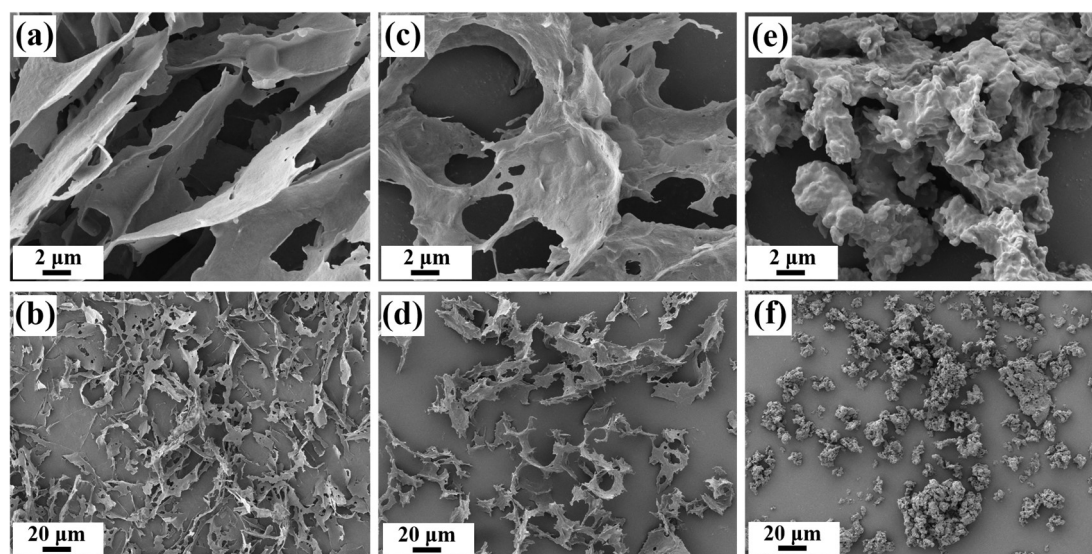
332

### 333 3.1.2 Fabrication of the thiol-rich and Sr<sup>2+</sup> imprinted hydrogel SA-PA-H

334 A three-step route was carried out to fabricate a thiol-rich and Sr<sup>2+</sup> imprinted SA-based  
335 hydrogel adsorbent as illustrated in Figure 1. The synthesis procedure has been described in  
336 section 2.2.2 and 2.2.3 in detail. The relatively low yield (37.2%) indicates incomplete reaction  
337 between SA-Sr and PA, that is, the SA-PA-H was far from being fully crosslinked. The unreacted  
338 hydroxyls and pendant chains in the hydrogels assure good hydrophilicity and enough free volume  
339 of the adsorbents for the diffusion of water molecules and Sr<sup>2+</sup> ions. FTIR was applied to examine  
340 the structures of the prepared SA-PA-Sr and SA-PA-H hydrogels (Figure 3b). In the spectrum of  
341 SA-PA-Sr, there were two carbonyl peaks at 1733 cm<sup>-1</sup> and 1631 cm<sup>-1</sup>. The peak at 1631 cm<sup>-1</sup> was  
342 ascribed to the vibration of C=O bonds in the carboxyl group, which is confirmed by the spectrum  
343 of SA containing only carboxyl groups rather than ester groups. Meanwhile, the C=O vibration  
344 peak at 1733 cm<sup>-1</sup> corresponded to ester carbonyl groups. The characteristic carbonyl absorption  
345 signal was absent in the spectrum of SA but observed in the spectrum of PA which was abundant  
346 with the ester group. The reduction of carboxyl absorption and the co-existence of the ester group  
347 and the carboxyl group suggested partial esterification of SA with PA. The unreacted carboxyl  
348 group was arguably due to the chelation of carboxyl groups with Sr<sup>2+</sup>, which prevented them from  
349 esterification. The esterification between carboxylic groups and hydroxyl groups was also

350 supported by a slightly decreased broad O-H absorption band in the range of 3000–3500  $\text{cm}^{-1}$  in  
351 SA-PA-Sr as compared with the spectrum of SA. On the other hand, S-H vibration signals were  
352 clearly observed in SA-PA-Sr indicating the existence of thiol groups in SA-PA-Sr. The FTIR  
353 spectrum demonstrated that SA-PA-Sr has the expected chemical structure. The partial  
354 esterification allowed SA-PA-Sr to be protonated to SA-PA-H as the intact ion-imprinted  
355 crosslinked hydrogel-bearing carboxyl group and thiol group as dual adsorption sites. In contrast,  
356 SA-Sr without covalent crosslinking would lose integrity in hydrochloric acid due to the break of  
357  $\text{Sr}^{2+}$  chelation.

358 Morphologies of SA-Sr, SA-PA-Sr and SA-PA-H were investigated by SEM (Figure 4). As  
359 Figure 4a&b displayed, the SA-Sr hydrogel was a well-defined porous network composed of  
360 layered structures with smooth surfaces. The micron-sized pores were likely to be the result of  
361 water loss from swelled hydrogel during the preparation of SEM samples. SA-PA-Sr was also a  
362 three-dimensional (3D) porous network composed of platelets (Figure 4c&d). However, the  
363 surface of the platelets is rougher and more porous than SA-Sr. The difference in the morphology  
364 could be explained by the modification of hydrogel by esterification crosslinking of SA and PA,  
365 which led to slightly contracted and wrinkled surfaces. After elution with acid, the hydrogel (SA-  
366 PA-H) has a morphology consisting of collapsed agglomerates (Figure 4 e&f). This is because in  
367 the SA-Sr and SA-PA-Sr hydrogels,  $\text{Sr}^{2+}$  acted as non-covalent crosslinkers, by complexing with  
368 carboxyl groups from different SA chains, to construct the 3D network structures of the hydrogels,  
369 which were however eliminated during the acid elution. The exchange of  $\text{Sr}^{2+}$  by proton largely  
370 reduced the number of the non-covalent crosslinkers, triggering partial agglomerates of the  
371 framework platelets. In spite of this, the SA-PA-H still maintained the form of hydrogel containing  
372 a large content of water (i.e. 94.4%) as demonstrated above. The morphology alternation confirms  
373 the efficient removal of the  $\text{Sr}^{2+}$  via acid elution, forming ion-imprinted cavities in the SA-PA-H  
374 as adsorption sites.



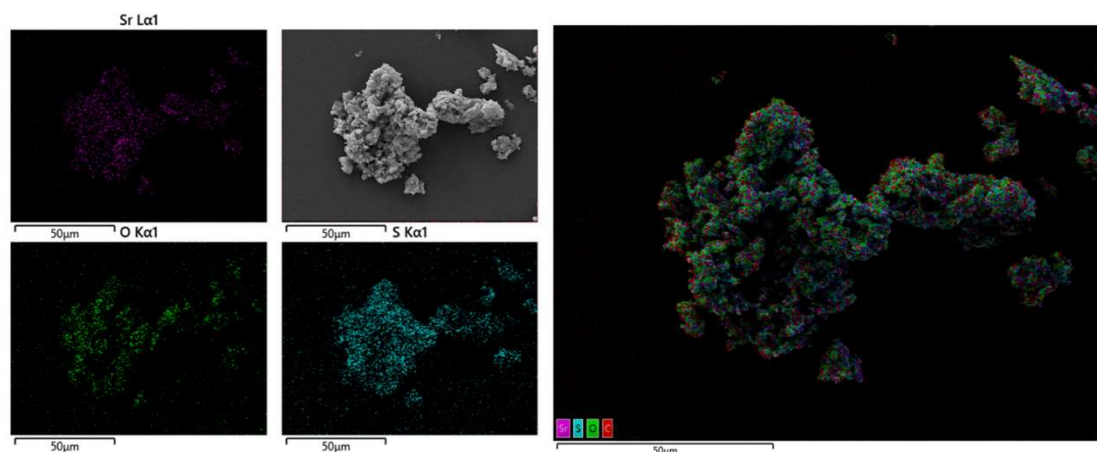
375

376 Figure. 4. SEM images of SA-Sr (a-b), SA-PA-Sr (c-d) and SA-PA-H (e-f) samples coated by gold  
377 and observed at different magnifications.

378

379 The distribution of Sr, O and S elements in SA-Sr (Figure S2), SA-PA-Sr (Figure S3) and  
380 SA-PA-H (Figure 5) hydrogels were further studied by SEM-EDX to confirm the successful  
381 synthesis of SA-PA-H composite hydrogels with Sr-imprinted moieties. In the EDX elemental  
382 map of SA-Sr (Figure S2), the intensity of S elements was barely stronger than the background  
383 noise. The observed trace amount of sulfur likely stemmed from sulfonic groups in the emulsifier  
384 AOT used during the preparation of SA-Sr hydrogel. After modification by PA, SA-PA-Sr and SA-  
385 PA-H hydrogel showed strong signals of S elements in its EDX elemental map (Figure S3&5),  
386 which indicated successful incorporation of PA along with abundant thiol groups into the  
387 hydrogels. For the Sr element, both EDX elemental maps of SA-Sr and SA-PA-Sr exhibited strong  
388 Sr signals (Figure S2&S3), implying the prevalence of  $\text{Sr}^{2+}$  adsorbed in the hydrogels. Compared  
389 with SA-Sr and SA-PA-Sr, the intensity of Sr element diminished obviously in the EDX elemental  
390 map of SA-PA-H (Figure 5). The results revealed that the majority of  $\text{Sr}^{2+}$  chelated in the hydrogel  
391 was removed by washing it with hydrochloric acid. The intensities of O elements remained almost  
392 unchanged through the preparation, suggesting backbones of the hydrogels remained stable. The  
393 EDX elemental mapping validated the successful fabrication of the thiol-rich and ion-imprinted  
394 SA-PA-H hydrogel adsorbent by the three-step protocol.



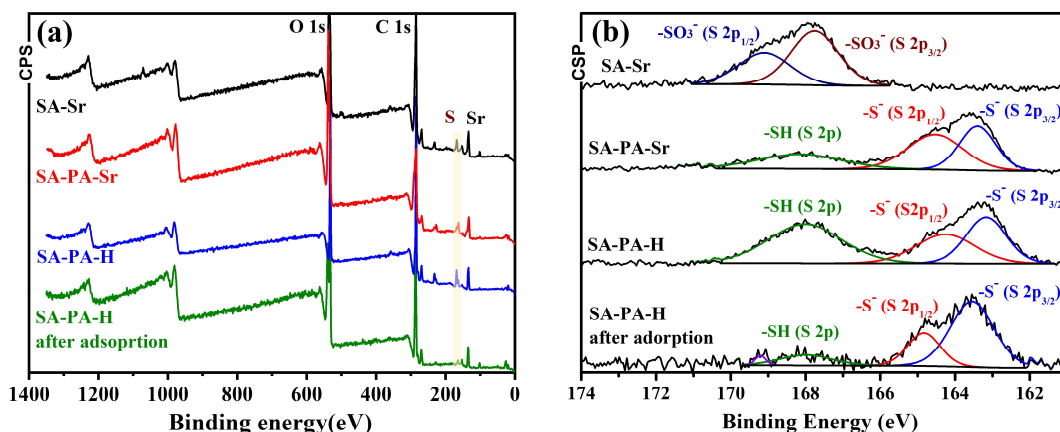


395

396 Figure. 5. EDX elemental maps along with the SEM image of SA-PA-H showing the distribution  
397 of Sr, O and S in the sample by purple, green and cyan, respectively.

398

399 To further reveal the composition and interaction between components (e.g. SA, PA and  $\text{Sr}^{2+}$ )  
400 in the composite hydrogels, XPS spectra (Figure 6) along with high-resolution S2p spectra (Figure  
401 6b) of the hydrogels were investigated. Due to spin-orbital coupling, deconvolution of every  
402 merged S2p peak presented closely coupled peaks ascribed to S2p<sub>1/2</sub> and S2p<sub>3/2</sub> photoelectron lines  
403 (Figure 6b). In the spectrum of SA-Sr hydrogel, the peaks at 169.1 and 167.7 eV can be assigned  
404 to the sulfonate ( $-\text{SO}_4^-$ ) group introduced by trace AOT during preparation. The existence of  
405 sulfonate peaks explained the trace sulfur signal in the EDX mapping of SA-Sr (Figure S2). After  
406 PA was added to SA-Sr followed by esterification, three deconvoluted S2p peaks with different  
407 binding energies at 168.2, 164.6 and 163.4 eV appeared in the XPS spectrum of SA-PA-Sr (Figure  
408 6b). The peaks at 164.6 and 163.4 eV originated from thiol anion S ( $-\text{S}^-$ ) chelating with  $\text{Sr}^{2+}$ , and  
409 the peak at 168.2 eV was attributed to protonated thiol group S ( $-\text{SH}$ ) without  $\text{Sr}^{2+}$  bonded, which  
410 overlapped with sulfonate peaks and was too weak to be deconvoluted to S2p<sub>1/2</sub> and S3p<sub>3/2</sub> peaks.  
411 The three characteristic peaks were also observed in the XPS spectrum of SA-PA-H (Figure 6b).  
412 However, the ratio between the integral area of the  $-\text{S}^-$  peaks over the area of the  $-\text{SH}$  peak  
413 decreased in SA-PA-H as compared to SA-PA-Sr, which indicated the dissociation of  $\text{Sr}^{2+}$  from  
414 sulfur and an increased amount of protonated sulfhydryl group. The results demonstrated that PA  
415 successfully modified the SA hydrogel and introduces sulfur sites for  $\text{Sr}^{2+}$  binding. By washing  
416 with acid, the  $\text{Sr}^{2+}$  was partially removed from SA-PA-Sr and the sulfhydryl group was recovered  
417 in SA-PA-H to serve as potential  $\text{Sr}^{2+}$  adsorption moieties.



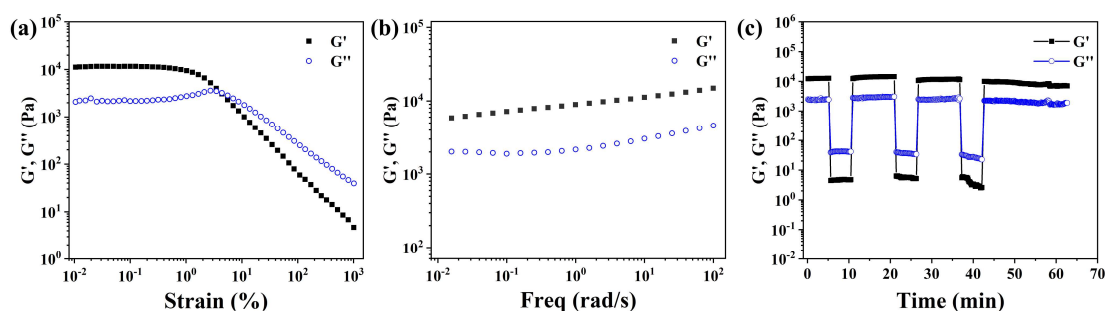
418  
 419 Figure 6. (a) XPS survey spectra of SA-Sr, SA-PA-Sr, SA-PA-H and SA-PA-H after adsorption of  
 420 Sr<sup>2+</sup>. The signals of electrons in O 1s, C 1s and Sr are labeled close to the corresponding peaks,  
 421 and the electron signal of S is highlighted by the yellow box. (b) High resolution XPS spectra of S  
 422 2p peaks of SA-Sr, SA-PA-Sr, SA-PA-H and SA-PA-H after adsorption of Sr<sup>2+</sup>. The S 2p peaks are  
 423 deconvoluted to separated peaks labeled with corresponding sulfur-containing groups.

424

### 425 3.2 Hydrogel rheology

426 The viscoelasticity of the SA-PA-H hydrogel was investigated for its further application as  
 427 membrane materials. The swollen hydrogel was subjected to a strain sweep test and a frequency  
 428 sweep test at room temperature ( T = 25 °C). The results are shown in Figure 7a&b. It is found that  
 429 the SA-PA-H is elastic as storage modulus (G') > loss modulus (G'') at small strain, while yield  
 430 beyond a critical strain where  $\gamma = 4.4\%$  and  $G' = G''$ . The frequency sweep confirmed that the SA-  
 431 PA-H is strongly elastic with  $G' \approx 10$  kPa, and  $G'$  is larger than  $G''$  throughout all shear  
 432 frequencies. The elasticity is ascribed to the network structure of SA-PA-H crosslinked by  
 433 esterification. Moreover, there would be massive hydrogen bonding formed between ester,  
 434 carboxyl, hydroxyl and thiol groups, which can further strengthen the hydrogel.

435



436 Figure 7. (a)  $G'$  and  $G''$  of SA-PA-H hydrogel in strain sweep test under oscillation shear at 1 rad/s  
437 frequency. (b) Frequency-dependent  $G'$  and  $G''$  of SA-PA-H under oscillation shear at a strain  
438 amplitude of 0.5%. (c) Step-strain behavior of SA-PA-H indicating a reversible recovery in  $G'$  and  
439  $G''$  at small strain (0.1%) after yielding at large strain (1000%).

440

441 A step-strain experiment was performed to demonstrate the self-recovery ability and the  
442 processability of the SA-PA-H hydrogel (Figure 7c), which was expected to be realized by  
443 reversible dissociation and reformation of non-covalent hydrogen bonds in the hydrogels. The  
444 swollen hydrogel was subjected to an oscillation shear by small strains (0.1%) and large strains  
445 (1000%) alternately and the result is shown in Figure 7c. Initially, the hydrogel was sheared at a  
446 small strain below the yield point, where  $\gamma = 0.1\%$  at  $\omega = 1.0$  rad/s. The  $G'$  and  $G''$  of the SA-PA-H  
447 are about 13 kPa and 2.4 kPa, respectively, indicating that the hydrogel is in a quasi-solid state. As  
448 the strain increased to 1000% beyond the yield point,  $G'$  and  $G''$  significantly decreased to  $\sim 4.4$  Pa  
449 and  $\sim 40$  Pa (i.e.  $\tan \delta \equiv G''/G' \sim 8.8-9.3$ ), respectively (Figure 7c), indicating the hydrogel was in a  
450 liquid state. Nevertheless, when the strain was decreased to 0.1%, the  $G'$  recovered to 13 kPa  
451 immediately and  $\tan \delta$  of the hydrogel decreased to 0.21 at the same time, revealing that the  
452 hydrogel recovered to a quasi-solid state. In the subsequent strain-step alternations, repeated  
453 yielding and recovery of the hydrogel were observed, demonstrating no significant loss in the  
454 viscoelasticity nor a change in the rate of structural reformation of the hydrogel even underwent  
455 repeated large strain deformations. Only a small drop of  $G'$  and  $G''$  was observed in the last strain-  
456 step test (4<sup>th</sup> cycle) due to the loss of water from the hydrogel after long-time measurement (Figure  
457 7c). The behavior demonstrated that SA-PA-H hydrogel can be readily processed and reshaped  
458 without damaging its mechanical properties thanks to the presence of massive hydrogen bonds  
459 between polymer chains. The robustness with strong elasticity allows us to reshape the fabricated  
460 hydrogel into membrane filtration devices for facile water purification, which will be discussed in  
461 section 3.3.5.

462

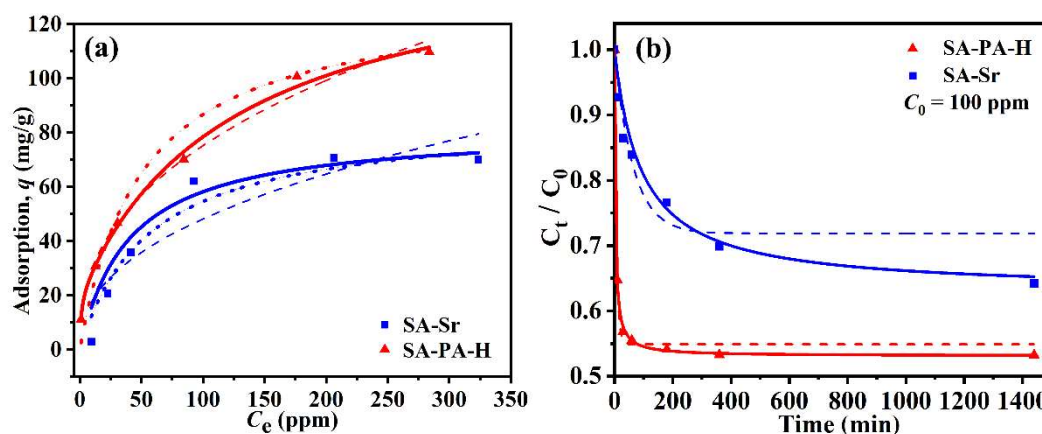
### 463 3.3 Strontium adsorption

#### 464 3.3.1 Isothermal adsorption

465 To investigate the ability of the hydrogels to remove radioactive  $\text{Sr}^{2+}$  from polluted water, we  
 466 examined the isothermal adsorption behavior of SA-PA-H and SA-Sr in simulated  $\text{Sr}^{2+}$  solutions.  
 467 The well-known Langmuir model was applied to describe  $\text{Sr}^{2+}$  adsorption behaviors, assuming: (i)  
 468 surface monolayer sorption, (ii) a finite number of binding sites, (iii) uniform sorption energies,  
 469 and (iv) no transmigration of sorbates in the plane of the surface. Adsorption ( $q$ , mg of adsorbate/g  
 470 of adsorbent) of  $\text{Sr}^{2+}$  by the hydrogels was plotted against equilibrium  $\text{Sr}^{2+}$  concentration ( $C_e$ , ppm)  
 471 in solution as shown in Figure 8a. The adsorption data were fitted by the Langmuir isotherm:

$$472 \quad q = \frac{bq_m C_e}{1 + bC_e} \quad (2)$$

473 where  $b$  is the Langmuir constant related to the affinity coefficient of binding sites (L/mg) and  $q_m$   
 474 is the maximum sorption capacity of  $\text{Sr}^{2+}$  for the adsorbent.



475 Figure 8. (a)  $\text{Sr}^{2+}$  adsorption isotherm with adsorption ( $q$ ) plotted against the equilibrium  
 476 concentration ( $C_e$ ) for SA-PA-H and SA-Sr. The dotted, solid and dashed lines are fittings  
 477 according to single-site Langmuir, dual-site Langmuir and Freundlich isotherm models,  
 478 respectively; (b)  $\text{Sr}^{2+}$  adsorption kinetics by SA-PA-H and SA-Sr at  $C_0 = 100$  ppm. The dashed and  
 479 solid lines are fittings according to PFORE and PSORE, respectively.  
 480

481  
 482 As shown in Figure 8a, the adsorption data of both SA-PA-H and SA-Sr can be fitted by  
 483 single-site Langmuir isotherm with a decent correlation coefficient (dotted lines,  $R^2 = 0.961$  and  
 484  $0.971$ , respectively). Table 1 lists the Langmuir fitting parameters,  $q_m$  and  $b$  of the hydrogels. As  
 485 can be seen, the SA-PA-H had an excellent adsorption capacity with a high  $q_m$  value of  $130.0$  mg/g.  
 486 In contrast, the  $q_m$  of SA-Sr is much lower ( $87.9$  mg/g) due to that a majority of the sorption sites  
 487 (e.g. the carboxyl groups in SA) were already occupied by  $\text{Sr}^{2+}$ . The adsorption results indicated

488 the importance of the Sr<sup>2+</sup>-imprinted cavities obtained via acid elution of the SA-PA-Sr to remove  
 489 pre-complexed Sr<sup>2+</sup> and of the thiol groups introduced by PA in enhancing the Sr<sup>2+</sup> adsorption  
 490 capacity of the SA-PA-H hydrogel.

491

492 Table 1. Single-site, dual-site Langmuir and Freundlich isotherm models for Sr<sup>2+</sup> adsorption

Sample	Langmuir model			dual-site Langmuir model					Freundlich model		
	$q_m$ (mg/g)	$b$ (L/mg)	$R^2$	$q_{m1}$ (mg/g)	$b_1$ (L/mg)	$q_{m2}$ (mg/g)	$b_2$ (L/mg)	$R^2$	$K_F$ (mg <sup>1-n</sup> •L <sup>n</sup> /g)	$n$	$R^2$
SA-PA-H	130.0	0.02	0.961	20.5	0.98	131.2	0.007	0.991	11.92	0.400	0.989
SA-Sr	87.9	0.01	0.971	25.7	0.01	62.2	0.011	0.939	6.750	0.427	0.813

493

494 Considering that in the SA-PA-Sr hydrogel both the ion-imprinted cavities located at the  
 495 carboxyl groups in SA chains and the thiol groups introduced from PA would contribute to the Sr<sup>2+</sup>  
 496 adsorption as different sorption sites with different sorption energies, the dual-site Langmuir  
 497 adsorption model was also used to fit the adsorption data:

$$498 \quad q = \frac{b_1 q_{m1} C_e}{1 + b_1 C_e} + \frac{b_2 q_{m2} C_e}{1 + b_2 C_e} \quad (3)$$

499 where the fitting parameters  $b_1$  and  $b_2$ , and  $q_{m1}$  and  $q_{m2}$  represent the affinity coefficients (L/mg)  
 500 and the maximum sorption capacity (mg/g) for the two types of sorption sites, respectively.

501 As shown in Figure 8a (the solid lines) and Table 1, the Dual-site Langmuir model better  
 502 described the adsorption behavior of the SA-PA-H with a higher  $R^2$  (0.991) than the single-site  
 503 Langmuir model (0.961). On the other hand, the adsorption data of SA-Sr was poorly fitted by the  
 504 dual-site Langmuir model ( $R^2 = 0.939$ ), suggesting that the SA-Sr was a single-site adsorbent  
 505 (Figure 8a). The fitting results validated the two sorption sites for Sr<sup>2+</sup> in the SA-PA-H hydrogel,  
 506 that is, the thiol group and the ion-imprinted carboxyl group, with a total maximum adsorption  
 507 capacity ( $q_m$ ) of 151.7 mg/g. This well meets the purpose of designing the SA-PA-H using ion-  
 508 imprinting and thiol-rich strategies to enhance the Sr<sup>2+</sup> adsorption performance. The role of the  
 509 thiol group was also confirmed by the XPS measurement of the SA-PA-H hydrogel after the  
 510 adsorption experiment. The peak ascribed to the thiol group (-SH) diminished while the peaks of  
 511 thiol anion (-S<sup>-</sup>) were amplified when compared to the signal before adsorption (Figure 6b),  
 512 confirming the adsorption of Sr<sup>2+</sup> to the thiol group by forming S<sup>-</sup>(1/2Sr<sup>2+</sup>) complex.

513 The adsorption data are also fitted to the Freundlich isotherm:

$$514 \quad q = K_F c_e^n \quad (4)$$

515 where  $K_F$  is the Freundlich sorption coefficient and  $n$  is the adsorption intensity [52].

516 As shown in Figure 8a (dashed lines), the Fredulich isotherm successfully captures the  
517 adsorption behaviors of SA-PA-H ( $R^2 = 0.989$ , Table 1) while it fails to fit the adsorption data of  
518 SA-Sr ( $R^2 = 0.813$ ). The Freundlich isotherm describes multilayer adsorption and assumes  
519 exponential decay in the energy distribution of heterogeneous adsorbed sites [52]. The excellent  
520 fitting of the Freundlich isotherm to SA-PA-H adsorption data but not the SA-Sr confirms the  
521 exsistence of more than one type of adsorption sites in SA-PA-H, that is, the carboxylic and thiol  
522 groups. This is consistent with the dual-site Langmuir model, and the values of  $n$  are lower than 1,  
523 indicating a nonlinear sorption on the adsorbents.

524 Moreover, to confirm the essential role of PA in the fabrication of highly efficient adsorbent,  
525 a control sample of  $\text{Sr}^{2+}$ -imprinted SA hydrogel without PA component, named SA-H, was  
526 prepared by eluting SA-Sr with hydrochloride acid, and its  $\text{Sr}^{2+}$  adsorption performance was  
527 evaluated, with data shown in Figure S4. Since the data failed to be fitted by Langmuir models  
528 (see discussion in the Supporting Information), the comparison of adsorption performance  
529 between SA-H and SA-PA-H, SA-Sr was done at given  $C_e$ s. The general trend clearly showed a  
530 worse adsorption capability of the SA-H than SA-PA-H. For example, at  $C_e = 250$  ppm, the  $q$  of  
531 SA-H was only 48 mg/g, while  $q$  of SA-PA-H was  $\sim 103.9$  mg/g. Surprisingly, at a given  $C_e$ , the  $q$   
532 of SA-H was even smaller than that of SA-Sr whose carboxyl groups had been chelated with  $\text{Sr}^{2+}$ .  
533 One possible reason was that during the acid elution, progressive esterification between carboxyl  
534 groups and hydroxyl groups in SA would occur as catalyzed by acid, which can significantly  
535 abolish the adsorption sites of carboxyl groups. In contrast, in the presence of PA, hydroxyl groups  
536 in SA had been consumed by esterification with carboxyl groups from PA. Thus, the carboxyl  
537 groups of SA were kept intact and imprinted by  $\text{Sr}^{2+}$  during the acid elution process, potentially  
538 acting as selective adsorption sites for  $\text{Sr}^{2+}$ . This indicates that PA is an indispensable modifier for  
539 SA to achieve the successful preparation of efficient  $\text{Sr}^{2+}$ -imprinted adsorbents.

540

541 3.3.2 Adsorption kinetics

542  $\text{Sr}^{2+}$  adsorption kinetics of SA-PA-H and SA-Sr were studied. As shown in Figure 8b, SA-PA-  
 543 H adsorbed  $\text{Sr}^{2+}$  in a very fast manner, with the adsorption equilibrium almost reached in 30 min.  
 544 In contrast,  $\text{Sr}^{2+}$  adsorption of SA-Sr was relatively slow, having the adsorption equilibrium even  
 545 not fully reached in the experiment time (12 h). To quantify the adsorption kinetics of the  
 546 hydrogels, the data were fitted by a pseudo-first order rate equation (PFORE) and a pseudo-second  
 547 order rate equation (PSORE):

$$548 \quad \log(q_e - q_t) = \log(q_e) - \frac{k_1}{2.303} t \quad (5)$$

$$549 \quad \frac{t}{q_t} = \frac{1}{k_2 q_e^2} + \frac{t}{q_e} \quad (4-6)$$

550 where  $q_t$  and  $q_e$  are adsorbed  $\text{Sr}^{2+}$  quantities (mg/g) at time  $t$  and equilibrium respectively, and  $k_1$   
 551 and  $k_2$  are a first order and a second order rate constant, respectively.

552 The fitting parameters are shown in Table 2. The PSORE fitted the adsorption kinetics of SA-  
 553 PA-H very well with  $R^2 > 0.99$ , while the PFORE failed to describe the adsorption kinetics of both  
 554 the SA-PA-H and the SA-Sr hydrogels. The possible reason for the preference to the PSORE  
 555 kinetics instead of PFORE kinetics is that the adsorption of a single  $\text{Sr}^{2+}$  is a second order reaction  
 556 involving physicochemical interactions between two phases, that is, a  $\text{Sr}^{2+}$  cation from solution  
 557 and a binding group, i.e. carboxylic or thiol group, from solid phase. In the fitting results based on  
 558 PSORE, significantly higher  $k_2$  ( $0.67 \text{ g mg}^{-1} \text{ min}^{-1}$ ) and  $q_e$  ( $46.9 \text{ mg g}^{-1}$ ) of SA-PA-H than SA-Sr  
 559 indicated an excellent adsorption activity of the SA-PA-H. The enhanced adsorption kinetics of the  
 560 SA-PA-H were attributed to the multiple sorption sites and the likely promotion by  $\text{Sr}^{2+}$ -imprinting  
 561 and the additional adsorption sites of thiol groups.

562

563 Table 2 Fitting parameters of PFORE and PSORE for  $\text{Sr}^{2+}$  sorption by SA-PA-H and SA-Sr

Sample	PSORE			PFORE		
	$k_2$ ( $\text{g mg}^{-1} \text{ min}^{-1}$ )	$q_e$ ( $\text{mg g}^{-1}$ )	$R^2$	$k_2$ ( $\text{g mg}^{-1} \text{ min}^{-1}$ )	$q_e$ ( $\text{mg g}^{-1}$ )	$R^2$
SA-PA-H	0.67	46.9	0.99	0.15	45.1	0.86
SA-Sr	0.03	37.0	0.91	0.02	28.1	0.69

564

565

566 3.3.3 pH and temperature effect



567 Polluted water from different resources might have various pH values and the temperature of  
568 the polluted water can also vary depending on the environment. Therefore, it is crucial to study the  
569 stability of the composite hydrogel when used to uptake  $\text{Sr}^{2+}$  in environments of different pH and  
570 temperatures to better guide its practical application in recovering  $\text{Sr}^{2+}$  from real wastewater.

571 For pH effect, adsorption experiments were carried out at  $C_o = 100$  ppm in a pH range from 2  
572 to 12 (Figure 9a). The adsorption behavior of SA-PA-H for  $\text{Sr}^{2+}$  are evaluated by the adsorption  
573 capacity and removal efficiency ( $E$ ). The filtration efficiency is evaluated by removal efficiency ( $E$ )  
574 calculated from equation (7):

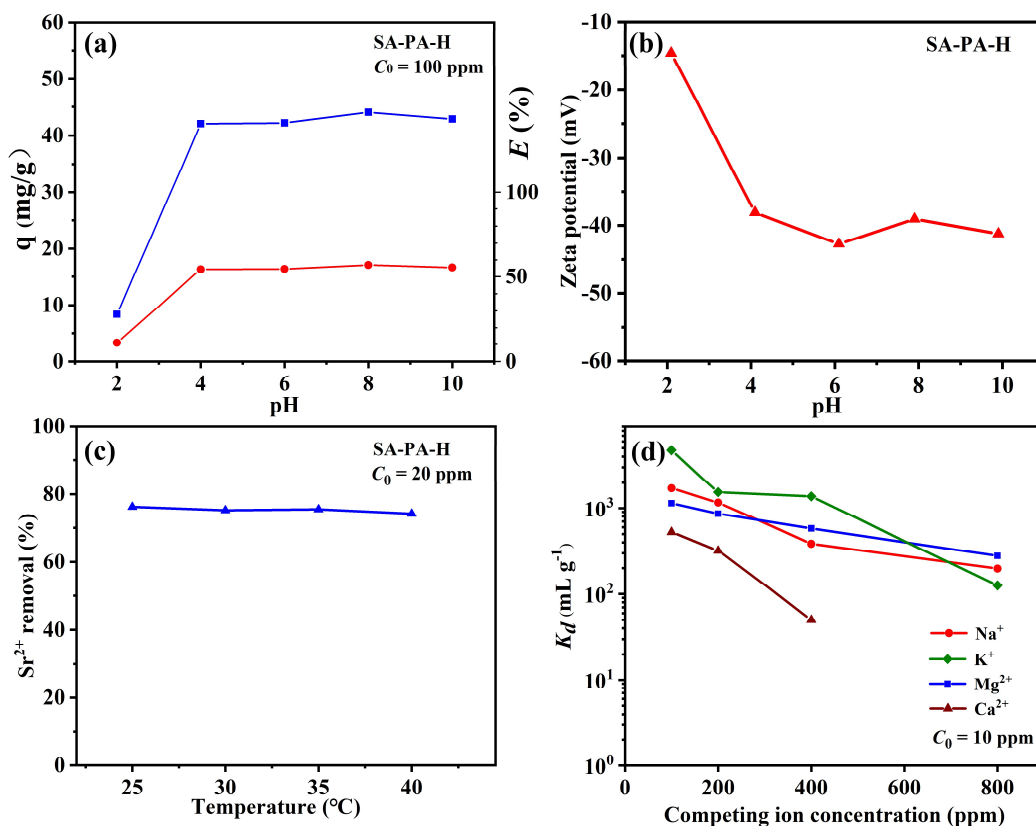
$$575 \quad E(\%) = \frac{C_o - C_e}{C_o} \times 100\% \quad (67)$$

576 where  $C_o$  and  $C_e$  are initial and equilibrium concentrations of  $\text{Sr}^{2+}$  measured by ICP-OES.

577 Over a wide range of pH (4-10), the sorption capacity of SA-PA-H towards  $\text{Sr}^{2+}$  was almost  
578 unchanged with a  $q \sim 41$  mg/g and a removal efficiency around 54%-57%. The SA-PA-H showed  
579 superior stability in solutions with various pH. However, when the solution pH was lowered to 2,  
580 the sorption capacity  $q$  dropped to 17.7 mg/g, only  $\sim 40\%$  of that of the other pH values. The  
581 suppressed adsorption here was owing to the high concentration of  $\text{H}^+$  competing with  $\text{Sr}^{2+}$  to bind  
582 with carboxyl groups. On the other hand, when suspended in a more basic  $\text{Sr}^{2+}$  solution with pH of  
583 12, the swollen SA-PA-Hs were observed to degrade into water soluble substances with the  
584 suspension becoming a clear solution. This is likely due to that the base environment catalyzed the  
585 hydrolysis of ester crosslinks in SA-PA-H, resulting in the degradation of the SA-PA-H into water  
586 soluble anionic SA and PA. Therefore, the adsorption of SA-PA-H at more alkaline pH cannot be  
587 evaluated, while the experiment demonstrated a possible way of degradation of the adsorbents  
588 after use.

589 To further elucidate the effect of  $\text{H}^+$  on SA-PA-H hydrogel, the Zeta potential of the hydrogel  
590 was measured (Figure 7b). When the pH value was greater or equal to 4, the majority of carboxyl  
591 groups in SA-PA-H were deprotonated and existed as carboxy anions, which negatively charged  
592 the surface of the hydrogel with a low Zeta potential around -40.0 mV. As the pH was decreased to  
593 2, the carboxyl groups in the hydrogel were protonated, resulting in an increase of the Zeta  
594 potential to -14.6 mV. The different states of the carboxyl groups revealed by the Zeta potential  
595 measurement demonstrated the important role of carboxy anion as available sites for  $\text{Sr}^{2+}$  sorption,

596 which could be modulated by pH to realize  $\text{Sr}^{2+}$  desorption and regeneration of the SA-PA-H  
 597 adsorbent.  
 598



599  
 600 Figure 9. The effect of pH, temperature and competing ions on SA-PA-H and its adsorption. (a)  
 601  $\text{Sr}^{2+}$  sorption capacity ( $q$ ) and  $\text{Sr}^{2+}$  removal efficiency at  $C_0 = 100$  ppm versus pH from 2-10; (b)  
 602 pH dependence of the Zeta potential of SA-PA-H versus pH from 2-10; (c)  $\text{Sr}^{2+}$  removal efficiency  
 603 at  $C_0 = 20$  ppm versus temperature from 25 °C to 40 °C; (d) Distribution coefficient  $K_d$  of  $\text{Sr}^{2+}$  ( $C_0$   
 604 = 10 ppm) in brine solutions containing  $\text{Na}^+$ ,  $\text{K}^+$ ,  $\text{Ca}^{2+}$  or  $\text{Mg}^{2+}$  for SA-PA-H plotted versus  
 605 concentration of the competing ions ranging from 200 ppm to 800 ppm. The adsorption of  $\text{Sr}^{2+}$  in  
 606 the presence of 800 ppm  $\text{Ca}^{2+}$  was undetected.

607

608 Temperature effect on the adsorption performance of SA-PA-H hydrogel was further studied  
 609 by testing  $\text{Sr}^{2+}$  adsorption behaviors of the SA-PA-H at temperatures from 25 °C to 40 °C (Figure  
 610 9c) in  $\text{Sr}^{2+}$  solutions with an initial concentration  $C_0 = 20$  ppm. As shown, for the measured  
 611 temperatures, the removal rate of  $\text{Sr}^{2+}$  by SA-PA-H remained consistent, more than 75%, almost  
 612 independent of the temperature. That is, the SA-PA-H hydrogel exhibited good temperature

613 stability within the range of 25-40 °C. Based on adsorption data at different temperatures, the  
614 thermodynamics parameters like Gibbs free energy ( $\Delta G^0$ ), enthalpy ( $\Delta H^0$ ) and entropy ( $\Delta S^0$ ) of  
615 the adsorption can be calculated from the following equations (8-10)[53]:

$$616 \quad K_a = \frac{q_e}{C_e} \quad (8)$$

$$617 \quad \ln K_a = \frac{\Delta S^0}{R} - \frac{\Delta H^0}{RT} \quad (9)$$

$$618 \quad \Delta G^0 = \Delta H^0 - T\Delta S^0 \quad (10)$$

619 where  $K_a$  is the distribution coefficient, which equals to the ratio between adsorption ( $q$ ) and  
620 equilibrium concentration of the solutes in the solution.  $R$  is the gas constant. By plotting  $\ln K_a$   
621 against  $1/T$ , the temperature-dependent adsorption data can be fitted by the *Van't Hoff* equation  
622 (Figure S5). The  $\Delta H^0$  and  $\Delta S^0$  are calculated to be -27.1 kJ/mol and -83.2 J/(mol·K), respectively.

623 The thermodynamics parameters obtained are listed in Table S2.

624 As seen in the results (Table S2), the negative  $\Delta H^0$  indicates that the adsorption of  $\text{Sr}^{2+}$  by  
625 SA-PA-H is exothermic, supported by the  $\text{Sr}^{2+}$  adsorption decline with increased temperature. On  
626 the other hand, the negative  $\Delta S^0$  shows an entropy reduction during the adsorption of  $\text{Sr}^{2+}$  by SA-  
627 PA-H, which can be a result of the configuration loss of carboxylic groups and thiol groups after  
628 binding with divalent ion  $\text{Sr}^{2+}$ . The negative  $\Delta G^0$  confirms that the adsorption occurs  
629 spontaneously under the tested conditions.

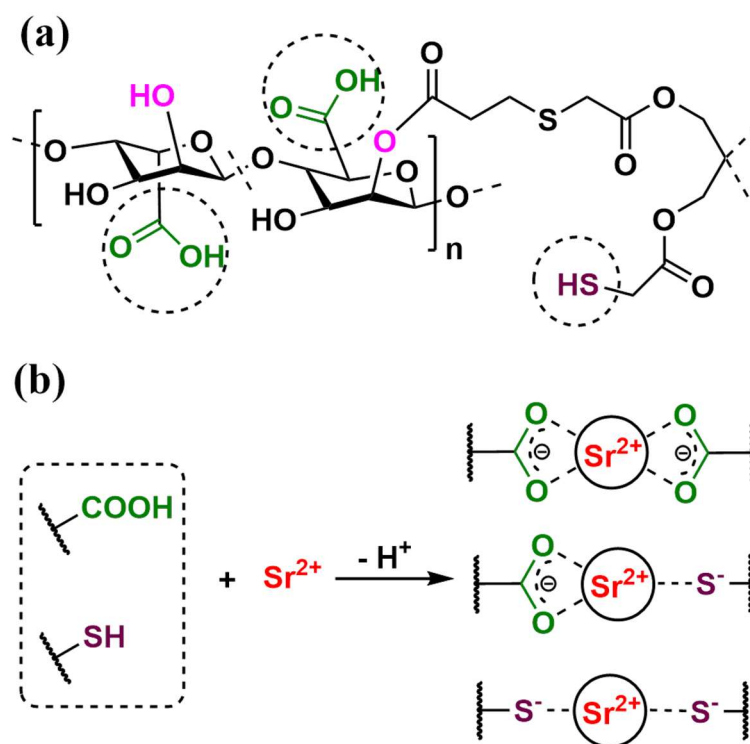
630 In summary, the adsorption of  $\text{Sr}^{2+}$  on SA-PA-H adsorbent is a spontaneous and endothermic  
631 process, even being efficient in complicated environments with various temperatures and pH.

632

### 633 3.3.4 Adsorption Mechanism

634 In sum of the isothermal adsorption, adsorption kinetics and thermodynamics studies, an  
635 adsorption mechanism is proposed. In the suspension of SA-PA-H, the SA-PA-H hydrogel is  
636 swollen by the water molecules with its functional groups hydrated in the medium (Figure 10a).  
637 The  $\text{Sr}^{2+}$  dissolved in the solution exchanges with protons from adsorption-active groups, *i.e.*,  
638 carboxylic and thiol groups within the ion-imprinted hydrogel. The generated Lewis bases,  
639 carboxylate and thiolate groups, serve as anionic ligands to fix  $\text{Sr}^{2+}$  in the ion-imprinted cavities  
640 whereby a single  $\text{Sr}^{2+}$  is chelated with two adsorbate groups, which could be two carboxylate

641 ligands, two thiolate ligands or a carboxylate ligand along with a thiolate ligand (Figure 10b). The  
 642 binding of  $\text{Sr}^{2+}$  by the thiols to form thiolate species can be demonstrated by the XPS spectrum of  
 643 SA-PA-H after adsorption (Figure 6b), where the -SH signals significantly diminished while an  
 644 enhanced  $\text{S}^-$  signal is observed compared to those in the SA-PA-H spectrum. Since the hydrogel is  
 645 demonstrated to be homogeneous with carboxylic and thiol groups distributed evenly within the  
 646 hydrogel by the EDX maps (Figure 5) and the hydrogel exhibits multilayer adsorption behavior  
 647 according to the fitting by the Freundlich model, it is arguably that the  $\text{Sr}^{2+}$  can be adsorbed by all  
 648 the active adsorption groups throughout the fully swollen porous hydrogel, where the diffusion of  
 649  $\text{Sr}^{2+}$  is less hindered.



650  
 651 Figure 10. (a) The chemical structure of SA-PA-H (PA-crosslinked alginic acid) with adsorption-  
 652 active carboxylic and thiol groups circled. (b) Ion exchange reaction between  $\text{Sr}^{2+}$  and protons in  
 653 carboxylic and thiol groups. A single  $\text{Sr}^{2+}$  is bound by two carboxylate ligands, two thiolate  
 654 ligands or a carboxylate ligand and a thiolate ligand.

655

### 656 3.3. 5 Competing ion effect

657 Sodium ( $\text{Na}^+$ ), potassium ( $\text{K}^+$ ), calcium ( $\text{Ca}^{2+}$ ) and magnesium ( $\text{Mg}^{2+}$ ) are the most common  
 658 competing ions for  $\text{Sr}^{2+}$  when adsorbents were used in real polluted water. To figure out the

659 adsorption selectivity of SA-PA-H towards  $\text{Sr}^{2+}$ , the hydrogel was dispersed in  $\text{Sr}^{2+}$  solutions ( $C_0 =$   
660 10 ppm) containing  $\text{Na}^+$ ,  $\text{K}^+$ ,  $\text{Ca}^{2+}$  or  $\text{Mg}^{2+}$  with varied ion concentrations from 100 to 800 ppm.  
661  $\text{Sr}^{2+}$  selectivity was evaluated by the distribution coefficient,  $K_d$ :

$$662 \quad K_d = \frac{C_0 - C_e}{C_e} \frac{V}{m} \quad (11)$$

663 where  $C_0$  and  $C_e$  are the initial and equilibrium concentrations of  $\text{Sr}^{2+}$ ,  $V$  is the volume (mL) of the  
664 solution, and  $m$  is the mass (g) of the absorbent.

665 The  $\text{Sr}^{2+}$  selectivity  $K_d$  was plotted against competing ion concentrations (Figure 9d). When  
666 the initial  $\text{Na}^+$  concentration was 100 ppm,  $K_d$  of SA-PA-H to  $\text{Sr}^{2+}$  was as high as  $1.72 \times 10^3 \text{ mL g}^{-1}$ .  
667 Although the  $K_d$  of SA-PA-H gradually decreased as the concentration of  $\text{Na}^+$  was increased, SA-  
668 PA-H still showed a good adsorption selectivity towards  $\text{Sr}^{2+}$  with a  $K_d$  of  $1.97 \times 10^2 \text{ mL g}^{-1}$  when  
669 the  $\text{Na}^+$  concentration reached 800 ppm (Figure 9d). The good selectivity to  $\text{Sr}^{2+}$  was also  
670 observed in the presence of  $\text{K}^+$  with  $K_d$  decreasing from  $4.27 \times 10^3 \text{ mL/g}$  to  $1.25 \times 10^2 \text{ mL/g}$  as the  
671 concentration of  $\text{K}^+$  increased from 100 to 800 ppm. Similarly, when the initial  $\text{Mg}^{2+}$  concentration  
672 was 100 ppm, the  $K_d$  towards  $\text{Sr}^{2+}$  was  $1.14 \times 10^3 \text{ mL g}^{-1}$ , which decreased to  $2.80 \times 10^2 \text{ mL g}^{-1}$  as  
673 the  $\text{Mg}^{2+}$  concentration reached 800 ppm (Figure 9d). On the other hand, SA-PA-H selectively  
674 adsorbs  $\text{Sr}^{2+}$  at low concentrations of  $\text{Ca}^{2+}$  (100-400 ppm) with  $K_d$ s from  $5.27 \times 10^2 \text{ mL/g}$  to 50  
675  $\text{mL/g}$ . However, when the  $\text{Ca}^{2+}$  is as high as 800 ppm, the adsorption of  $\text{Sr}^{2+}$  by SA-PA-H is minor.  
676 Since there is a few  $\text{Sr}^{2+}$  remaining in SA-PA-H after acid wash, the remained  $\text{Sr}^{2+}$  may exchange  
677 with  $\text{Ca}^{2+}$  who is in overwhelming excess in the competing adsorption test. Thus, the adsorption of  
678  $\text{Sr}^{2+}$  in the presence of high concentrations (e.g. 800 ppm) of  $\text{Ca}^{2+}$  was suppressed, which may be  
679 resolved by washing the SA-PA-H hydrogel with acids for more times. All in all, the experiments  
680 demonstrated the decent selectivity of SA-PA-H to  $\text{Sr}^{2+}$  over most competing ions ( $\text{Na}^+$ ,  $\text{K}^+$  and  
681  $\text{Mg}^{2+}$ ) except  $\text{Ca}^{2+}$  at high concentrations. The selectivity was attributed to the thiol group and the  
682 ion-imprinting involved in the hydrogel. According to the hard and soft acids and bases (HSAB)  
683 principle[45], both strontium and sulfur are ‘soft’ atoms with thick electronic cloud be easy to  
684 deform because of their large atomic numbers. Thus, the thiol group was prone to bind with  $\text{Sr}^{2+}$   
685 instead of  $\text{Na}^+$ ,  $\text{K}^+$  and  $\text{Mg}^{2+}$  which are regarded as ‘hard’ cations. Meanwhile, ion-imprinting  
686 created cavities with specific shapes and ligand distribution adapted to the geometry and charge  
687 distribution of  $\text{Sr}^{2+}$ , acting as ion sieves for  $\text{Sr}^{2+}$ . Since Sr, Ca and Mg are alkaline-earth metal

688 elements with the same bivalent charge when presented as cations, the volume of ion-imprinted  
689 cavities was expected to play an essential role in selectively recovering  $\text{Sr}^{2+}$  from concentrated  
690  $\text{Mg}^{2+}$  solutions or diluted  $\text{Ca}^{2+}$  solutions in light of the size exclusion effect of the cavities. The  
691 two factors contributed together to the good selectivity of SA-PA-H towards  $\text{Sr}^{2+}$ .

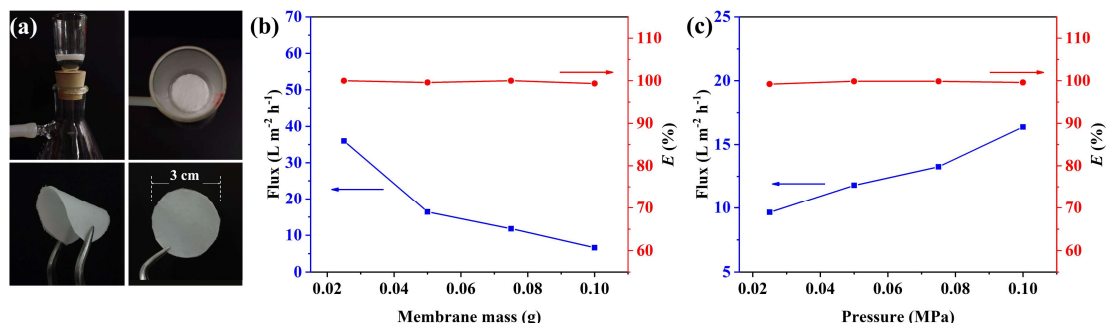
692

### 693 3.3.6 Membrane filtration

694 Membrane filtration is an advanced technique for desalination and water purification with several  
695 advantages such as low cost, facile operation and ready portability.[54-56] The rheological study  
696 in section 3.2 has demonstrated that the SA-PA-H hydrogel was recoverable after large  
697 deformation, which enables SA-PA-H to accommodate certain shapes for device filtrations. A  
698 simple vacuum membrane filtration device was established by depositing swollen SA-PA-H  
699 hydrogels onto the sand core in a suction funnel equipped with a suction bottle (Figure 10a). The  
700 adsorption efficiency of the SA-PA-H membrane was investigated under vacuum filtration  
701 conditions, where 100 mL  $\text{Sr}^{2+}$  solution with a  $C_0$  of 1 ppm passed through the membrane driven  
702 by vacuum.

703 After the filtration, a trace amount of  $\text{Sr}^{2+}$  was detected in the effluent in all the conditions  
704 (Figure S6), and the ion was removed completely after filtration by SA-PA-H membrane in all the  
705 conditions with extremely high removal efficiency ( $> 99.2\%$ ) (Figure 10b&c), which revealed the  
706 excellent adsorption efficiency of SA-PA-H in fast water purification. Varying the mass of SA-PA-  
707 H fabricating the membrane did not affect the removal efficiency of the membrane, and a  
708 complete removal ( $> 99.99\%$ ) of  $\text{Sr}^{2+}$  was achieved with only 0.025 g SA-PA-H (Figure 10b). An  
709 increased mass of SA-PA-H to 0.1 g decreased the water flux from  $36.0 \text{ L m}^{-2} \text{ h}^{-1}$  to  $6.6 \text{ L m}^{-2} \text{ h}^{-1}$   
710 because of augmented resistance due to the thicker membrane. When the trans-membrane pressure  
711 was raised from 0.025 MPa to 0.1 MPa (Figure 10c), the flux increased accordingly from  $9.6 \text{ L m}^{-2} \text{ h}^{-1}$   
712 to  $16.4 \text{ L m}^{-2} \text{ h}^{-1}$  while the removal efficiency remained unimpaired ( $> 99.2\%$ ). The flux can  
713 be readily regulated to produce pure water at desired rates without risks of unexpected percolation  
714 of solutes. The excellent membrane filtration performance is undoubtedly ascribed to the large  
715 adsorption capacity and the fast adsorption equilibrium of the SA-PA-H. Moreover, after the  
716 filtration the SA-PA-H membrane can be recovered from the suction funnel entirely and after

717 drying in the air it maintained as a free-standing membrane that can be bent elastically (Figure  
 718 10a). The good mechanical property in the dry state grants SA-PA-H great potential in fabricating  
 719 portable and disposable membranes for transportation and large-scale application.



720  
 721 Figure 11. (a) Device consisted of a filtration funnel for vacuum membrane filtration and external  
 722 appearance of a dried SA-PA-H membrane fabricated in its plat and bent forms. (b) Variation of  
 723 solution flux (square, left axis) and removal efficiency (circle, right axis) as a function of  
 724 membrane mass ranging from 0.02 to 0.1 g in membrane filtration experiments. (c) Variation of  
 725 solution flux (square, left axis) and removal efficiency (circle, right axis) as a function of trans-  
 726 membrane pressure ranging from 0.02 to 0.1 MPa in membrane filtration experiments.

727

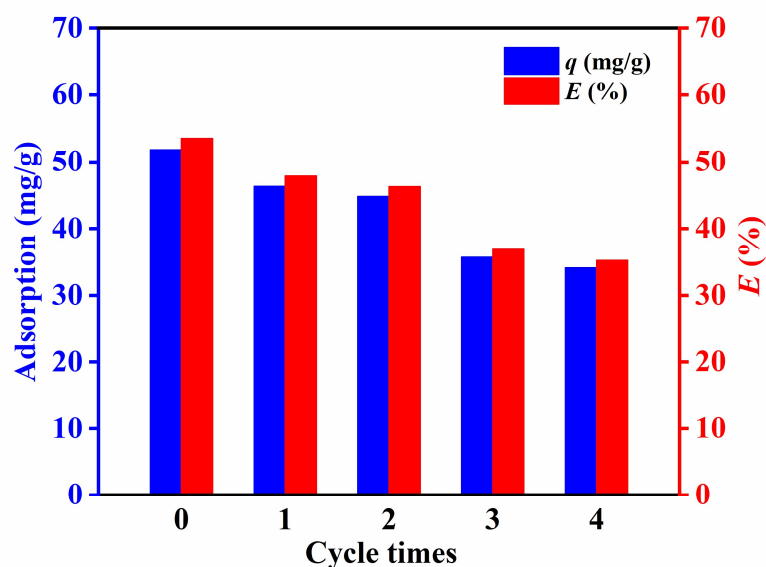
### 728 3.3.7 Recyclability

729 Adsorption and desorption of Sr<sup>2+</sup> are essential to the service life of adsorbents. An  
 730 economical and environment friendly adsorbent is expected to have good recyclability and  
 731 stability. To assess the recyclability and stability of the SA-PA-H adsorbent, Sr<sup>2+</sup> was removed  
 732 from the saturated adsorbent by hydrochloric acid to recover sorption sites after one batch  
 733 adsorption experiment. Then the regenerated adsorbent was subject to a new adsorption  
 734 experiment with the same initial Sr<sup>2+</sup> concentration ( $C_0 = 100$  ppm). In every adsorption cycle,  
 735 adsorption efficiency ( $E$ ) was calculated by equation (7).

736 As Figure 11 shows, the  $E$  of freshly-prepared SA-PA-H was 53.51% and the adsorption  
 737 capacity ( $q$ ) was 51.8 mg/g. In the first, second, third and fourth desorption-adsorption cycle,  $E$  of  
 738 regenerated adsorbents dropped slightly to 47.83%, 46.28%, 36.88% and 35.22%, respectively.  
 739 The attenuation of adsorption efficiency was only about 10%-20% in every regeneration taking the  
 740 hydrogel in the last cycle as the reference, indicating decent stability of the hydrogel. Since there  
 741 was an unavoidable loss of SA-PA-H hydrogel content during the recycling involving



742 centrifugation, the actual recycle efficiency was expected to be higher than the experimental  
743 values. The loss of adsorption capacity may also be attributed to the deterioration of adsorption  
744 sites resulting from the acid-catalyzed esterification between hydroxyl and carboxylic groups  
745 during acid wash in the regeneration step. The results showed that through washing with acids SA-  
746 PA-H adsorbent could be regenerated conveniently. In the meantime, protonation of the hydrogels  
747 released the adsorbed  $\text{Sr}^{2+}$  into the acid solutions, which enables an efficient separation of  $\text{Sr}^{2+}$   
748 from the contaminated water. The robustness allowed SA-PA-H to serve as a recyclable and  
749 environment friendly adsorbent to recover  $\text{Sr}^{2+}$  from polluted water with little waste and reagent  
750 contamination.



751  
752 Figure 12.  $\text{Sr}^{2+}$  adsorption capacity and adsorption efficiency ( $E$ ) of SA-PA-H hydrogel in batch  
753 adsorption experiments with an initial  $\text{Sr}^{2+}$  concentration of 100 ppm as a function of regeneration  
754 time. The SA-PA-H used was regenerated by washing the adsorbents with 100 mL 0.5 mol/L  
755 hydrochloric acid.

756

### 757 3.3.8 Comparison of adsorption performance

758 Table 3 compares the as-developed SA-based adsorbent with other reported adsorbents. As  
759 shown, the SA-PA-H hydrogel is among the most effective  $\text{Sr}^{2+}$  adsorbents in terms of maximum  
760 adsorption capacity. Moreover, the SA-PA-H adsorbent can reach adsorption equilibrium by a fast  
761 uptake kinetics and it is also sufficiently flexible to be shaped or loaded to fit different devices.  
762 These features enabled its application in continuous water purification processes such as column

763 filtration and membrane filtration, where the contact time between contaminated water and the  
764 adsorbent is very limited that the adsorbents with slow uptake kinetics fail to achieve good  
765 purification. Although there are adsorbents having significantly high adsorption capacity and short  
766 equilibrium time, they are mostly in form of powder, difficult to be applied in real water treatment  
767 because of their low availability to be fitted into common purification devices and the difficulties  
768 of post-treatment after adsorption (e.g. easily causing secondary pollution). Taking advantage of  
769 excellent adsorption efficiency, good selectivity, good pH stability and outstanding modality, SA-  
770 PA-H is a promising adsorbent candidate for real water treatment.

771

772 Table 3 Comparison of the adsorbent developed in this work with other Sr<sup>2+</sup> adsorbents reported.

Adsorbent	State	q <sub>max</sub> (mg/g)	Equilibrium (min)	pH range	Reference
Na Titanate	powder	49.6	60	3-10	[24]
polyantimonic acid- polyacrylonitrile (PAA-PAN)	powder	49	500	n. a.	[23]
Graphene oxide (GO)	powder	131.4	20	3-11	[22]
Covalent triazine polymer- Fe <sub>3</sub> O <sub>4</sub> (CTP-Fe <sub>3</sub> O <sub>4</sub> )	powder	128	200	7-14	[31]
layered vanadosilicate (SGU- 7)	powder	109	10	3-13	[57]
Na <sub>2</sub> Sn <sub>3</sub> S <sub>7</sub> (NaTS)	powder	80.0	1	3-13	[46]
K <sub>1.87</sub> ZnSn <sub>1.68</sub> S <sub>5.30</sub> (KZTS)	powder	19.3	1	3-11	[47]
Na <sub>5</sub> Zn <sub>3.5</sub> Sn <sub>3.5</sub> S <sub>13</sub> ·6H <sub>2</sub> O (NaZTS)	powder	40.40	5	3-12	[49]
Impregnated nano-zeolite (NAASMS-Z)	powder	350	30	7-10	[26]
K <sub>2</sub> Sb <sub>4</sub> S <sub>7</sub> ·2H <sub>2</sub> O (SbS-1K)	powder	61.1	40	4-11	[58]
Thioglycolic acid-modified alginate sodium (SA-TGA)	microsphere	177.37	180	4-8	[44]
metakaolin/slag-based zeolite (M/SZMs)	microsphere	54.90	30	4-8	[59]
Chitosan	Fiber and microsphere	20.0	200	3-7	[60]
Graphene oxide/Nickel-metal- organic framework composite (GO/Ni-MOF)	membrane	72	>500	n.a.	[61]
Bacterial cellulose membrane modified with ethylenediaminetetraacetic acid (BCM@APTES-EDTA)	membrane	44.86	600	n.a.	[30]
SA-PA-H	moldable hydrogel	151.7	30	4-10	This work

773

#### 774 4 Conclusion

775 A Sr<sup>2+</sup>-imprinted and thiol-functionalized hydrogel based on SA (*i.e.* SA-PA-H) was successfully  
776 synthesized and used to selectively adsorb Sr<sup>2+</sup> from contaminated water. The synthesis of  
777 hydrogel involved three steps including the formation of SA hydrogel in emulsion via  
778 complexation with Sr<sup>2+</sup>, crosslinking of the alginate gels via esterification with thiol-  
779 functionalized tetra-arm carboxylic acids (PA), and lastly activation by acid elution to form Sr<sup>2+</sup>-  
780 imprinted cavities. The synthesis route was verified by a series of techniques including NMR,  
781 FTIR, XPS and SEM, etc.

782 The incorporation of abundant thiol groups and the imprinted cavities with predetermined sizes  
783 endow the prepared SA-PA-H hydrogel with an excellent adsorption ability and decent selectivity  
784 towards Sr<sup>2+</sup> within a wide range of pH (4-10) and temperature (25-40 °C). The adsorption process  
785 followed second-order kinetics at an adsorption rate constant of 0.669 g mg<sup>-1</sup> min<sup>-1</sup>. The  
786 isothermal adsorption behavior can be well described by the dual-site Langmuir model with a  
787 maximum adsorption capacity of 151.7 mg g<sup>-1</sup>. The Sr<sup>2+</sup> binding to thiol and carboxyl groups has  
788 been confirmed to be the two main adsorption mechanisms. The selectivity was validated by that  
789 the existence of competing ions such as Mg<sup>2+</sup>, K<sup>+</sup> and Na<sup>+</sup> hardly weakened the adsorption  
790 efficiency of SA-PA-H to Sr<sup>2+</sup>, having a  $K_d$  greater than 1.97×10<sup>2</sup> mL/g obtained even at high  
791 competing ion concentrations.

792 Rheological investigation reveals that SA-PA-H hydrogel can self-recover after being damaged by  
793 large strains. The hydrogel can be easily fabricated into membranes for Sr<sup>2+</sup> separation with high  
794 removal efficiency (> 99.2%) within a wide range of liquid flux. The SA-PA-H adsorbent can be  
795 readily regenerated by washing with HCl solutions and the regenerated adsorbents possess  
796 comparable adsorption capability as the pristine hydrogel. The research developed a facile way to  
797 fabricate alginate-based hydrogel adsorbent for selective Sr<sup>2+</sup> separation. Thanks to its outstanding  
798 adsorption capability and good mechanical properties, SA-PA-H is promising in strontium  
799 recovery for contaminated water treatment.

800

801

802 **Acknowledgements**

803 This research was financially supported by the National Natural Science Foundation of China  
804 (22172028; 21903015; and 22111530080), the Natural Science Foundation of Fujian Province of  
805 China (2020J01145 and 2022J05041), the Award Program of Fujian Minjiang Scholar  
806 Professorship (2018) and the European Union's "Horizon 2020" research and innovation  
807 programme under the Marie Skłodowska-Curie Grant Agreement No. 844286(M4WASTE).

808

809 **Appendix A. Supplementary data**

810 Supplementary data to this article can be found online at: XXXX

811

812 **AUTHOR INFORMATION**813 **Corresponding Authors**

814 \*E-mail: [huagui.zhang@fjnu.edu.cn](mailto:huagui.zhang@fjnu.edu.cn) (H. Zhang)

815 **Author Contributions**

816 #B. Zheng and J. Yin contributed equally to this work.

817 **Notes**

818 The authors declare no competing interest.

819

820 **Reference**

- 821 [1] I. Smičiklas, M. Jović, M. Šljivić-Ivanović, V. Mrvić, D. Čakmak, S. Dimović, Correlation of  
822 Sr<sup>2+</sup> retention and distribution with properties of different soil types, *Geoderma* 253-254  
823 (2015) 21-29. [10.1016/j.geoderma.2015.04.003](https://doi.org/10.1016/j.geoderma.2015.04.003).
- 824 [2] Z. Begum, I. Rahman, T. Takase, H. Hasegawa, Formation and stability of the mixed-chelator  
825 complexes of Sr<sup>2+</sup>, Mg<sup>2+</sup>, Ca<sup>2+</sup>, Ba<sup>2+</sup>, and Y<sup>3+</sup> in solution with bio-relevant chelators, *J. Inorg.*  
826 *Biochem.* 195 (2019) 141-148. <https://doi.org/10.1016/j.jinorgbio.2019.03.018>.
- 827 [3] Y. Li, S. Le, Z. Wang, Y. Hong, K. Li, Q. Pu, Preparation and characterization of the Sr<sup>2+</sup>-  
828 doped  $\gamma$ -Ce<sub>2</sub>S<sub>3</sub>@c-SiO<sub>2</sub> red pigments exhibiting improved temperature and acid stability, *Appl.*  
829 *Surf. Sci.* 508 (2020) 145266-145273. <https://doi.org/10.1016/j.apsusc.2020.145266>.
- 830 [4] K. Xu, W. Chen, G. Fu, X. Mou, R. Hou, Y. Zhu, K. Cai, In situ self-assembly of graphene  
831 oxide/polydopamine/Sr<sup>2+</sup> nanosheets on titanium surfaces for enhanced osteogenic  
832 differentiation of mesenchymal stem cells, *Carbon* 142 (2019) 567-579.
- 833 [5] J. Boonlakhorn, N. Chanlek, P. Thongbai, P. Srepusharawoot, Strongly enhanced dielectric  
834 response and structural investigation of (Sr<sup>2+</sup>, Ge<sup>4+</sup>) co-doped CCTO ceramics, *J. Phys.*  
835 *Chem. C* 124 (2020) 20682-20692.
- 836 [6] C. Chen, T. Xuan, W. Bai, T. Zhou, F. Huang, A. Xie, L. Wang, R. Xie, Highly stable CsPbI<sub>3</sub>:  
837 Sr<sup>2+</sup> nanocrystals with near-unity quantum yield enabling perovskite light-emitting diodes  
838 with an external quantum efficiency of 17.1%, *Nano Energy* 85 (2021) 106033.

- 839 <https://doi.org/10.1016/j.nanoen.2021.106033>.
- 840 [7] X. Liu, Z. Ren, T. Yang, Y. Hao, Q. Wang, J. Zhou, Tunable dielectric metamaterial based on  
841 strontium titanate artificial atoms, *Scripta Mater.* 184 (2020) 30-33.  
842 <https://doi.org/10.1016/j.scriptamat.2020.03.041>.
- 843 [8] T. Su, Z. Han, Z. Qu, Y. Chen, X. Lin, S. Zhu, R. Bian, X. Xie, Effective recycling of Co and  
844 Sr from Co/Sr-bearing wastewater via an integrated Fe coagulation and hematite precipitation  
845 approach, *Environ. Res.* 187 (2020) 109654-109662.  
846 <https://doi.org/10.1016/j.envres.2020.109654>.
- 847 [9] S. Mane, S. Ponrathnam, N. Chavan, Selective solid-phase extraction of metal for water  
848 decontamination, *J. Appl. Polym. Sci.* 133 (2016) 42849. 10.1002/app.42849.
- 849 [10] H. Zhang, S. Tangparitkul, B. Hendry, J. Harper, Y.K. Kim, T.N. Hunter, J.W. Lee, D.  
850 Harbottle, Selective separation of cesium contaminated clays from pristine clays by flotation,  
851 *Chem. Eng. J.* 355 (2019) 797-804. 10.1016/j.cej.2018.07.135.
- 852 [11] J. Xu, H. Qiao, K. Yu, M. Chen, C. Liu, W. Richtering, H. Zhang, Cu<sup>2+</sup> tunable temperature-  
853 responsive Pickering foams stabilized by poly (N-isopropylacrylamide-co-vinyl imidazole)  
854 microgel: Significance for Cu<sup>2+</sup> recovery via flotation, *Chem. Eng. J.* 442 (2022) 136274.  
855 10.1016/j.cej.2022.136274.
- 856 [12] L. Zhu, D. Zhu, Y. Sheng, J. Xu, D. Harbottle, H. Zhang, Polydopamine-coated magnetic  
857 montmorillonite immobilized with potassium copper hexacyanoferrate for selective removal  
858 of Cs<sup>+</sup> and its facile recovery, *Appl. Clay Sci.* 216 (2022). 10.1016/j.clay.2021.106367.
- 859 [13] H. Zhang, C.S. Hodges, P.K. Mishra, J.Y. Yoon, T.N. Hunter, J.W. Lee, D. Harbottle, Bio-  
860 Inspired Preparation of Clay-Hexacyanoferrate Composite Hydrogels as Super Adsorbents for  
861 Cs(I), *ACS Appl. Mater. Interfaces* 12 (2020) 33173-33185. 10.1021/acsami.0c06598.
- 862 [14] C.R. Minitha, R. Suresh, U.K. Maity, Y. Haldorai, V. Subramaniam, P. Manoravi, M. Joseph,  
863 R.T. Rajendra Kumar, Magnetite Nanoparticle Decorated Reduced Graphene Oxide  
864 Composite as an Efficient and Recoverable Adsorbent for the Removal of Cesium and  
865 Strontium Ions, *Ind. Eng. Chem. Res.* 57 (2018) 1225-1232.  
866 <https://doi.org/10.1021/acs.iecr.7b05340>.
- 867 [15] Y.C. Zou, L. Mogg, N. Clark, C. Bacaksiz, S. Milovanovic, V. Sreepal, G.P. Hao, Y.C. Wang,  
868 D.G. Hopkinson, R. Gorbachev, S. Shaw, K.S. Novoselov, R. Raveendran-Nair, F.M. Peeters,  
869 M. Lozada-Hidalgo, S.J. Haigh, Ion exchange in atomically thin clays and micas, *Nat. Mater.*  
870 20 (2021) 1677-1682. 10.1038/s41563-021-01072-6.
- 871 [16] E. Han, Y. Kim, H. Yang, I. Yoon, M. Choi, Synergy between zeolite framework and  
872 encapsulated sulfur for enhanced ion-exchange selectivity to radioactive cesium, *Chem. Mater.*  
873 30 (2018) 5777-5785. <http://doi.org/10.1021/acs.chemmater.8b02782>.
- 874 [17] P. Khan, A. Bhattacharyya, J. Sharma, S. Manohar, The recovery of strontium from acidic  
875 medium using novel strontium selective extractant: An experimental and DFT study, *J. Hazard.*  
876 *Mater.* 397 (2020) 122476-122484. <https://doi.org/10.1016/j.jhazmat.2020.122476>.
- 877 [18] S. Younis, R. El-Salamony, Y. Tsang, K. Kim, Use of rice straw-based biochar for batch  
878 sorption of barium/strontium from saline water: protection against scale formation in  
879 petroleum/desalination industries, *J. Clean. Prod.* 250 (2020) 119442-119450.  
880 <https://doi.org/10.1016/j.jclepro.2019.119442>.
- 881 [19] H. Kim, Y. Kang, Y. Lee, S. Choi, J. Lim, J. Lee, Automated extraction chromatographic  
882 radionuclide separation system for analysis of <sup>90</sup>Sr in seawater, *Talanta* 217 (2020) 121055-

- 883 121063. <https://doi.org/10.1016/j.talanta.2020.121055>.
- 884 [20] M. Feng, D. Sarma, Y. Gao, X. Qi, W. Li, X. Huang, M.G. Kanatzidis, Efficient removal of  
885  $[UO_2]^{2+}$ ,  $Cs^+$ , and  $Sr^{2+}$  ions by radiation-resistant gallium thioantimonates, *J. Am. Chem. Soc.*  
886 140 (2018) 11133-11140. <https://doi.org/10.1021/jacs.8b07457>.
- 887 [21] B. Park, S. Ghoreishian, Y. Kim, B. Park, S. Kang, Y. Huh, Dual-functional micro-adsorbents:  
888 application for simultaneous adsorption of cesium and strontium, *Chemosphere* 263 (2021)  
889 128266-128275. <https://doi.org/10.1016/j.chemosphere.2020.128266>.
- 890 [22] A. Abu-Nada, A. Abdala, G. McKay, Isotherm and Kinetic Modeling of Strontium Adsorption  
891 on Graphene Oxide, *Nanomaterials* 11 (2021) 2780-2790.  
892 <https://doi.org/10.3390/nano11112780>.
- 893 [23] F. Ma, Z. Li, W. Zhou, Q. Li, L. Zhang, Application of polyantimonic acid-polyacrylonitrile  
894 for removal of strontium (II) from simulated high-level liquid waste, *J. Radioanal. Nucl.*  
895 *Chem.* 311 (2017) 2007-2013.
- 896 [24] C. Li, C. Liu, L. Chen, Z. Ye, Y. Zhang, X. Wang, Y. Wei, Studies on the separation and in-situ  
897 sintering solidification of strontium by a highly-efficient titanate-based adsorbent, *Micropor.*  
898 *Mesopor. Mater.* 288 (2019) 109607-109615.  
899 <https://doi.org/10.1016/j.micromeso.2019.109607>.
- 900 [25] S. Kwon, C. Kim, E. Han, H. Lee, H. Cho, M. Choi, Relationship between zeolite structure  
901 and capture capability for radioactive cesium and strontium, *J. Hazard. Mater.* 408 (2021)  
902 124419. <https://doi.org/10.1016/j.jhazmat.2020.124419>.
- 903 [26] H. Hassan, O.A. Moamen, W. Zaher, Adaptive Neuro-Fuzzy inference system analysis on  
904 sorption studies of strontium and cesium cations onto a novel impregnated nano-zeolite, *Adv.*  
905 *Powder Technol.* 31 (2020) 1125-1139. <https://doi.org/10.1016/j.appt.2019.12.031>.
- 906 [27] T. Shubair, O. Eljamal, A. Tahara, Y. Sugihara, N. Matsunaga, Preparation of new magnetic  
907 zeolite nanocomposites for removal of strontium from polluted waters, *J. Mol. Liq.* 288 (2019)  
908 111026-111036. <https://doi.org/10.1016/j.molliq.2019.111026>.
- 909 [28] N. Ghaeni, M.S. Taleshi, F. Elmi, Removal and recovery of strontium (Sr (II)) from seawater  
910 by Fe<sub>3</sub>O<sub>4</sub>/MnO<sub>2</sub>/fulvic acid nanocomposite, *Mar. Chem.* 213 (2019) 33-39.
- 911 [29] J. Choi, Y. Park, S. Choi, Synthesis of metal-organic framework ZnO<sub>x</sub>-MOF@MnO<sub>2</sub>  
912 composites for selective removal of strontium ions from aqueous solutions, *ACS Omega* 5  
913 (2020) 8721-8729. <https://doi.org/10.1021/acsomega.0c00228>.
- 914 [30] R. Cheng, M. Kang, S. Zhuang, L. Shi, X. Zheng, J. Wang, Adsorption of Sr (II) from water  
915 by mercerized bacterial cellulose membrane modified with EDTA, *J. Hazard. Mater.* 364  
916 (2019) 645-653.
- 917 [31] A. Rengaraj, Y. Haldorai, P. Puthiaraj, S.K. Hwang, T. Ryu, J. Shin, Y.-K. Han, W.-S. Ahn, Y.S.  
918 Huh, Covalent Triazine Polymer-Fe<sub>3</sub>O<sub>4</sub> Nanocomposite for Strontium Ion Removal from  
919 Seawater, *Ind. Eng. Chem. Res.* 56 (2017) 4984-4992. [10.1021/acs.iecr.7b00052](https://doi.org/10.1021/acs.iecr.7b00052).
- 920 [32] T. Lu, Y. Zhu, W. Wang, Y. Qi, A. Wang, Polyaniline-functionalized porous adsorbent for Sr<sup>2+</sup>  
921 adsorption, *J. Radioanal. Nucl. Chem.* 317 (2018) 907-917. [10.1007/s10967-018-5935-9](https://doi.org/10.1007/s10967-018-5935-9).
- 922 [33] S. Thakur, B. Sharma, A. Verma, J. Chaudhary, S. Tamulevicius, V.K. Thakur, Recent progress  
923 in sodium alginate based sustainable hydrogels for environmental applications, *J. Clean. Prod.*  
924 198 (2018) 143-159. [10.1016/j.jclepro.2018.06.259](https://doi.org/10.1016/j.jclepro.2018.06.259).
- 925 [34] J. Yang, Y. Xie, W. He, Research progress on chemical modification of alginate: A review,  
926 *Carbohydr. Polym.* 84 (2011) 33-39. <https://doi.org/10.1016/j.carbpol.2010.11.048>.



- 927 [35] X. Gao, C. Guo, J. Hao, Z. Zhao, H. Long, M. Li, Adsorption of heavy metal ions by sodium  
928 alginate based adsorbent-a review and new perspectives, *Int. J. Biol. Macromol.* 164 (2020)  
929 4423-4434.
- 930 [36] S.R. Choe, Y. Haldorai, S.-C. Jang, M. Rethinasabapathy, Y.-C. Lee, Y.-K. Han, Y.-S. Jun, C.  
931 Roh, Y.S. Huh, Fabrication of alginate/humic acid/Fe-aminoclay hydrogel composed of a  
932 grafted-network for the efficient removal of strontium ions from aqueous solution, *Environ.*  
933 *Technol. Inno.* 9 (2018) 285-293. <https://doi.org/10.1016/j.eti.2017.12.008>.
- 934 [37] S. Foster, N. Ramanan, B. Hanson, B. Mishra, Binding mechanism of strontium to biopolymer  
935 hydrogel composite materials, *J. Radioanal. Nucl. Chem.* (2022).  
936 <https://doi.org/10.1007/s10967-022-08613-6>.
- 937 [38] D. Fila, Z. Hubicki, D. Kołodyńska, Applicability of new sustainable and efficient alginate-  
938 based composites for critical raw materials recovery: General composites fabrication  
939 optimization and adsorption performance evaluation, *Chem. Eng. J.* 446 (2022).  
940 <https://doi.org/10.1016/j.cej.2022.137245>.
- 941 [39] A.S. Eltaweil, E.M. Abd El-Monaem, H.M. Elshishini, H.G. El-Aqapa, M. Hosny, A.M.  
942 Abdelfatah, M.S. Ahmed, E.N. Hammad, G.M. El-Subruiti, M. Fawzy, A.M. Omer, Recent  
943 developments in alginate-based adsorbents for removing phosphate ions from wastewater: a  
944 review, *RSC Adv* 12 (2022) 8228-8248. <http://doi.org/10.1039/d1ra09193j>.
- 945 [40] V. Kusumkar, M. Galambos, E. Viglasova, M. Dano, J. Smelkova, Ion-Imprinted Polymers:  
946 Synthesis, Characterization, and Adsorption of Radionuclides, *Materials* 14 (2021) 1083.  
947 <https://doi.org/10.3390/ma14051083>.
- 948 [41] L. Qin, Y. Zhao, L. Wang, L. Zhang, S. Kang, W. Wang, T. Zhang, S. Song, Preparation of ion-  
949 imprinted montmorillonite nanosheets/chitosan gel beads for selective recovery of Cu(II) from  
950 wastewater, *Chemosphere* 252 (2020) 126560.  
951 <https://doi.org/10.1016/j.chemosphere.2020.126560>.
- 952 [42] X. Luo, B. Guo, J. Luo, F. Deng, S. Zhang, S. Luo, J. Crittenden, Recovery of Lithium from  
953 Wastewater Using Development of Li Ion-Imprinted Polymers, *ACS Sustainable Chemistry &*  
954 *Engineering* 3 (2015) 460-467. 10.1021/sc500659h.
- 955 [43] D. Sun, Y. Zhu, M. Meng, Y. Qiao, Y. Yan, C. Li, Fabrication of highly selective ion imprinted  
956 macroporous membranes with crown ether for targeted separation of lithium ion, *Sep. Purif.*  
957 *Technol.* 175 (2017) 19-26. 10.1016/j.seppur.2016.11.029.
- 958 [44] C. Liu, X. Yu, C. Ma, Y. Guo, T. Deng, Selective recovery of strontium from oilfield water by  
959 ion-imprinted alginate microspheres modified with thioglycollic acid, *Chem. Eng. J.* 410  
960 (2021) 128267. 10.1016/j.cej.2020.128267.
- 961 [45] R. Pearson, Hard and soft acids and bases, *J. Am. Chem. Soc.* 85 (1963) 3533-3539.  
962 <https://doi.org/10.1021/ja00905a001>.
- 963 [46] Z. Zhang, P. Gu, M. Zhang, S. Yan, L. Dong, G. Zhang, Synthesis of a robust layered metal  
964 sulfide for rapid and effective removal of Sr<sup>2+</sup> from aqueous solutions, *Chem. Eng. J.* 372  
965 (2019) 1205-1215. <https://doi.org/10.1016/j.cej.2019.04.193>.
- 966 [47] M. Zhang, P. Gu, Z. Zhang, J. Liu, L. Dong, G. Zhang, Effective, rapid and selective  
967 adsorption of radioactive Sr<sup>2+</sup> from aqueous solution by a novel metal sulfide adsorbent,  
968 *Chem. Eng. J.* 351 (2018) 668-677. 10.1016/j.cej.2018.06.069.
- 969 [48] Y.M. Zhao, M. Sun, L. Cheng, K.Y. Wang, Y. Liu, J.Y. Zhu, S. Zhang, C. Wang, Efficient  
970 removal of Ba(2+), Co(2+) and Ni(2+) by an ethylammonium-templated indium sulfide ion

- 971 exchanger, J. Hazard. Mater. 425 (2022) 128007.  
972 <https://doi.org/10.1016/j.jhazmat.2021.128007>.
- 973 [49] M. Zhang, P. Gu, S. Yan, L. Dong, G. Zhang, Na/Zn/Sn/S (NaZTS): Quaternary metal sulfide  
974 nanosheets for efficient adsorption of radioactive strontium ions, Chem. Eng. J. 379 (2020).  
975 10.1016/j.cej.2019.122227.
- 976 [50] W. Mu, S. Du, Q. Yu, X. Li, H. Wei, Y. Yang, S. Peng, Highly efficient removal of radioactive  
977  $^{90}\text{Sr}$  based on sulfonic acid-functionalized  $\alpha$ -zirconium phosphate nanosheets, Chem. Eng. J.  
978 361 (2019) 538-546. <https://doi.org/10.1016/j.cej.2018.12.110>.
- 979 [51] A. James, S. Harding, T. Robshaw, N. Bramall, M. Ogden, R. Dawson, Selective  
980 environmental remediation of strontium and cesium using sulfonated hyper-cross-linked  
981 polymers (SHCPs), ACS Appl. Mater. Inter. 11 (2019) 22464-22473.  
982 <https://doi.org/10.1021/acsami.9b06295>.
- 983 [52] S. Kalam, S.A. Abu-Khamsin, M.S. Kamal, S. Patil, Surfactant Adsorption Isotherms: A  
984 Review, ACS Omega 6 (2021) 32342-32348. <http://doi.org/10.1021/acsomega.1c04661>.
- 985 [53] G.D. Değermenci, N. Değermenci, V. Ayvaoglu, E. Durmaz, D. Çakır, E. Akan, Adsorption of  
986 reactive dyes on lignocellulosic waste; characterization, equilibrium, kinetic and  
987 thermodynamic studies, J. Clean. Prod. 225 (2019) 1220-1229.  
988 <http://doi.org/10.1016/j.jclepro.2019.03.260>.
- 989 [54] A. Zapata-Sierra, M. Cascajares, A. Alcayde, F. Manzano-Agugliaro, Worldwide research  
990 trends on desalination, Desalination 519 (2021) 115305. 10.1016/j.desal.2021.115305.
- 991 [55] H. Zhang, S. Zhu, J. Yang, A. Ma, W. Chen, Enhanced removal efficiency of heavy metal ions  
992 by assembling phytic acid on polyamide nanofiltration membrane, Journal of Membrane  
993 Science 636 (2021) 119591. 10.1016/j.memsci.2021.119591.
- 994 [56] H. Xiang, X. Min, C. Tang, M. Sillanpää, F. Zhao, Recent advances in membrane filtration for  
995 heavy metal removal from wastewater: A mini review, J. Water Process Eng. 49 (2022)  
996 103023. <https://doi.org/10.1016/j.jwpe.2022.103023>.
- 997 [57] S. Datta, P. Oleynikov, W. Moon, Y. Ma, A. Mayoral, H. Kim, C. Dejoie, M. Song, O. Terasaki,  
998 K. Yoon, Removal of  $^{90}\text{Sr}$  from highly  $\text{Na}^+$ -rich liquid nuclear waste with a layered  
999 vanadosilicate, Energ. Environ. Sci. 12 (2019) 1857-1865.  
1000 <https://doi.org/10.1039/C8EE03302A>.
- 1001 [58] Y. Zhao, L. Cheng, K. Wang, X. Hao, J. Wang, J. Zhu, M. Sun, C. Wang, pH-Controlled  
1002 Switch over Coadsorption and Separation for Mixed  $\text{Cs}^+$  and  $\text{Sr}^{2+}$  by an Acid-Resistant  
1003 Potassium Thioantimonate, Adv. Funct. Mater. 32 (2022) 2112717.  
1004 <https://doi.org/10.1002/adfm.202112717>.
- 1005 [59] H. Lei, Y. Muhammad, K. Wang, M. Yi, C. He, Y. Wei, T. Fujita, Facile fabrication of  
1006 metakaolin/slag-based zeolite microspheres (M/SZMs) geopolymer for the efficient  
1007 remediation of  $\text{Cs}^+$  and  $\text{Sr}^{2+}$  from aqueous media, J. Hazard. Mater. 406 (2021) 124292.  
1008 10.1016/j.jhazmat.2020.124292.
- 1009 [60] S. Zhuang, K. Zhu, L. Xu, J. Hu, J. Wang, Adsorption of  $\text{Co}^{2+}$  and  $\text{Sr}^{2+}$  in aqueous solution by  
1010 a novel fibrous chitosan biosorbent, Sci. Total Environ. 825 (2022) 153998.  
1011 10.1016/j.scitotenv.2022.153998.
- 1012 [61] J. Cheng, K. Liu, X. Li, L. Huang, J. Liang, G. Zheng, G. Shan, Nickel-metal-organic  
1013 framework nanobelt based composite membranes for efficient  $\text{Sr}^{2+}$  removal from aqueous  
1014 solution, Environmental Science and Ecotechnology 3 (2020) 100035.

1015            10.1016/j.ese.2020.100035.

1016

1017